Fitful but sustained rupture of the 2026 M_w 7.6 Venezuela earthquake

Jeremy Wing Ching Wong[1*,2], Eitan Rapaport Bruck[1], Rubi Garcia Gonzalez[1], Mathilde Marchandon[3], Baoning Wu[1], Fabian Kutschera[1], Molly Zebker[1], Yohai Magen[1], Wenyuan Fan[1], Yuri Fialko[1], Alice-Agnes Gabriel[1,3]

[1]Scripps Institution of Oceanography, University of California San Diego, San Diego, United States of America.

[2]Université Côte d'Azur, IRD, CNRS, Observatoire de la Côte d'Azur, Géoazur, Sophia Antipolis, Valbonne, France.

[3] Department of Earth and Environmental Sciences, Ludwig-Maximilians-Universität München, Munich, Germany

[*]Corresponding author. Email: jeremywong@ucsd.edu

The devastating 2026 Venezuela earthquake was cataloged as a doublet of M_w 7.2 and 7.5 events. Combining NISAR and ALOS-2 Synthetic Aperture Radar data, teleseismic source imaging, and ensemble Kalman inversion of multiple moment tensors and dynamic rupture simulations, we show that the 2026 Venezuela earthquake was instead a single M_w 7.6 event with variable rupture speed and seismic moment release. The earthquake rupture went through episodes of acceleration and deceleration, including a pronounced slow-down around the rupture area of the 1967 M_w 6.6 Caracas earthquake. Stress transfer from the partially arrested front and a trailing slip pulse enabled the rupture to break through this stress barrier and release ~ 26% of the seismic moment beneath the coastal cities of Playa Grande and Caraballeda, where damage was most severe. Such fitful ruptures enhance high-frequency seismic radiation and challenge conventional methods for characterization of large earthquakes.

On 24 June 2026 at 18:04 local time (22:04 UTC), a destructive earthquake struck northern Venezuela, causing widespread damage across several north-central states, particularly in the coastal communities of La Guaira, including Playa Grande and Caraballeda (Fig. 1**A**). The event was reported as an earthquake doublet [1, 2] consisting of a moment-magnitude M_w7.2–7.3 event near San Felipe followed 32 s later by an M_w7.4–7.5 event offshore La Guaira. A doublet of M_w 7.2 and 7.5 earthquakes would imply two distinct ruptures with characteristic lengths of ~90 and 150 km and rupture durations of ~30–50 s, respectively [3]. Here we show that the available data and dynamic models are more consistent with a single M_w 7.6 rupture that propagated unilaterally over ~220 km in 70 s, with pronounced eastward directivity, toward the populated coast of La Guaira. The two interpretations imply different rupture dimensions, directivity, and stress changes imposed on adjacent fault segments, with important consequences for rapid source characterization and seismic-hazard assessment [4–7].

The 2026 Venezuela event propagated across two major fault systems, the Boconó and San Sebastián faults, whose connectivity throughout the seismogenic zone is poorly known [8, 9]. Continental strike-slip fault systems commonly contain bends, stepovers, junctions, and fault segments with varying orientations relative to the regional tectonic stress field [10, 11]. These geometrical variations modify the shear and normal stresses resolved onto the fault and can slow down, accelerate, redirect, or arrest a propagating rupture [12–16]. Whether a major bend acts as a persistent rupture barrier depends not only on its geometry and loading conditions, but also on the dynamic and static stress perturbations carried by the rupture into the geometric transition [17–21].

Here we show that the 2026 Venezuela earthquake was a single, connected rupture with pronounced variations in rupture speed, moment release, and high-frequency radiation. We integrate inversions of space geodetic data for the static slip distribution, Ensemble Kalman Inversion-Multi-Centroid-Moment-Tensor (EKI-MultiCMT) source imaging, and teleseismic backprojection to resolve a continuous eastward rupture over ~220 km across the Boconó–San Sebastián Fault system. We show that the rupture accelerated during the first ~40 s, subsequently slowed down to ~1 km/s for ~20 s, and finally re-accelerated toward La Guaira, accompanied by strong variations in moment release and high-frequency radiation. We use EKI 3D dynamic rupture simulations to identify the physical drivers of this multi-stage rupture. The orientation of the fault bend relative to the regional stress field promoted propagation across the fault junction at velocities near the

shear-wave speed, whereas a low-stress barrier near the epicentral area of the 1967 Caracas earthquake strongly decelerated the rupture. Stress transfer from the arrested front and a trailing slip pulse subsequently enabled rupture to propagate through the barrier. Together, our observations and numerical simulations reveal how fault geometry, inherited stress heterogeneity, and dynamic stress transfer produce a single connected rupture with strongly variable rupture speed and seismic radiation.

Regional tectonics

Northern Venezuela lies along the Caribbean–South American plate boundary, where the relative eastward motion of the Caribbean Plate at a rate of ~18–20 mm/yr is accommodated by dextral faulting and crustal shortening [8, 9, 22]. The 2026 earthquake propagated through the transition between the northeast-striking Boconó Fault and the east–west-striking San Sebastián Fault (Fig. 1A). The Boconó–San Sebastián–El Pilar fault system accommodates right-lateral motion with the fault slip rate increasing from west to east from approximately 10 to 17-18 mm/yr [9, 23]. Regional stress inversions indicate a transpressional strike-slip regime, which we approximate with a clockwise rotation of the maximum horizontal compressive stress, S_{Hmax}, from 130° to 145° eastward [24]. This combined variation in fault strike and stress orientation changes the resolved absolute stresses along the rupture. The fault system is seismogenic with several historical earthquakes, including the 1812 sequence, the 1900 M_w 7.6–7.7 Caracas earthquake, and the 1967 M_w ~6.6 Caracas earthquake [25].

Three distinct asperities along the Boconó–San Sebastián fault system

We investigate static coseismic displacements due to the 2026 Venezuela earthquake using radar and optical satellite observations (see Methods and Supplemental Materials). We combine the Interferometric Synthetic Aperture Radar (InSAR) [26] data from the NASA-ISRO NISAR and JAXA ALOS-2 missions to provide continuous maps of surface displacements from multiple lines of sight and a complete three-component displacement field [27, 28]. The coseismic displacement field (Fig. 2A) reveals a deformation pattern indicative of dextral slip on a ~ 220 km-long strike-slip rupture extending from the northeastern Boconó Fault onto the San Sebastián Fault. Horizontal

surface displacements do not exhibit notable variations between the inferred source regions of the M_w 7.2-7.5 earthquake doublet cataloged by the USGS [1], suggesting a continuous slip distribution along the entire source region. The largest coseismic displacements slightly over 1 m are observed along the northern Venezuelan coast, where the rupture trace goes onshore near the towns of Playa Grande and Caraballeda (Fig. 2A-C). Independent pixel-offset measurements from NISAR and Sentinel-1 radar amplitude images, together with Sentinel-2 and PlanetScope optical images, reveal large step-like displacements across the fault near Playa Grande and Caraballeda (Fig. 2B, C; Methods). The fault offsets become more localized toward the east side of Playa Grande and in Caraballeda (Fig. S8).

We synthesize geophysical and geological datasets to construct a 3D fault geometry (Methods Sec. "Constructing subsurface fault geometry"). The inferred fault geometry follows the northeast-striking Boconó Fault in the west and the approximately east-west-striking San Sebastián Fault in the east. We invert the NISAR and ALOS-2 LOS displacements for a static slip distribution using the inferred fault geometry and a layered elastic half-space model constrained by the regional seismic velocity structure (Table S2) with piece-wise linear triangular dislocation elements [29, 30].

The best-fit finite-fault slip model (Fig. 2D) reproduces surface displacement data with a variance reduction of $\sim$ 95%. The equivalent moment magnitude is M_w7.6, in agreement with the cumulative magnitude of the M_w7.2 and 7.5 doublet reported by the USGS [1]. Our model suggests three main asperities: the first one at ~20 km depth near the hypocentral area along the northeastern Boconó Fault; the second one in the middle of the ruptured section of the San Sebastián Fault, with peak slip up to 2.3 m near the surface, extending 75 km along-strike and 27 km depth; the third one located farther east around the town of Caraballeda with peak slip up to 2.6 m near the surface and extending 27 km along-strike and 15 km down-dip. The third asperity lies beneath Caraballeda, one of the two areas with the most severe recorded damage. The static slip model favors a single continuous rupture model, but does not explain how rupture propagated through the fault bend or generated the strongly variable seismic radiation.

Multistage rupture acceleration and deceleration

We investigate the spatiotemporal rupture evolution using Ensemble Kalman Multiple Centroid Moment Tensor Inversion (EKI-MultiCMT,[31]) and teleseismic P-wave backprojection [32], jointly constraining the low-frequency moment release and high-frequency seismic radiation. EKI-MultiCMT represents the earthquake as a sequence of distinct subevents without prescribing fault geometry or rupture speed. Using teleseismic P, SH, and surface-wave displacement records from 36 stations, we reconstructed the timing, location, focal mechanism, and moment release of each subevent. Backprojection uses 1272 teleseismic P-wave velocity records filtered at 0.2–1.0 Hz to image coherent high-frequency radiation with finer spatiotemporal resolution, particularly sensitive to changes in rupture propagation.

Our EKI-MultiCMT inversion reveals a multi-stage rupture that includes seven subevents over ~80 s and ~220 km between 68.6°W and 66.8°W, with a waveform variance reduction of up to 80% (Fig. 3). During the first ~40 s, the rupture produced relatively weak teleseismic P-wave signals, with displacement and velocity amplitudes less than half those of the subsequent 40–80 s phase (Fig. 3B, S12). To prevent the stronger later signals from dominating the inversion, we first constrain the early rupture using the initial 40 s of P waves and subsequently incorporate those results into a joint inversion of the full P, SH, and surface wave records (Methods Sec. "Ensemble Kalman Multiple Centroid Moment Tensor Inversion"). The first stage contains four spatially and temporally connected subevents that propagated unilaterally from the Boconó fault onto the San Sebastián Fault, releasing a cumulative moment equivalent to M_w 7.31 (1.18×10^{20} Nm, Fig.3D). The first three subevents exhibit a gradual strike rotation following the fault bend, while their apparent migration speed increases from ~ 2.1 km/s (1.0–2.6 km/s) to 3.8 km/s (3.6–4.3 km/s) by 40 s, approaching or locally exceeding the mid-crust shear wave speed of 3.65 km/s (Fig.3F, Table S2).

Following the initial acceleration, the rupture entered a slower, more episodic phase between ~40 and 70 s. Subevents 5 and 6 exhibit apparent migration speeds of only 0.8–1.0 km/s, accompanied by a pronounced reduction in moment release between 50 and 58 s. The rupture subsequently re-accelerated eastward to 2.7 km/s (2.0–3.2 km/s) during the final subevent near Caraballeda at ~65 s. The three later subevents released a cumulative moment equivalent to M_w 7.22 (8.42×10^{19} N m),

yielding a total magnitude of M_w 7.48 (2.02×10^{20} N m). Moment magnitude estimates depend on the trade-off between radiation patterns, source duration, spatial location, and Earth structure used [31]. All seven subevents exhibit strike-slip focal mechanisms consistent with right-lateral motion on a subvertical fault.

Teleseismic P-wave backprojection provides an independent reconstruction of rupture propagation by tracking the spatiotemporal migration of high-frequency radiation (Fig 3A,E,F; Methods Sec. Backprojection; [32–34]). The radiators initially migrated eastwards at subshear speeds, accelerating to near or above shear-wave speed between 20 and 40 s. Between 40 and 60 s, the high-frequency radiation becomes spatially concentrated, indicating a pronounced deceleration in radiator migration, before resuming eastward propagation at near shear-wave speed between 60 and 80 s. The radiators generally migrate slightly ahead of the moment-release centroids inferred from EKI-MultiCMT, providing complementary constraints on rupture propagation.

Together, EKI-MultiCMT and backprojection reveal a single connected rupture with multiple stages of moment release and high-frequency radiation. EKI-MultiCMT and the USGS finite-fault model indicate sustained moment release during the initial ~40 s, followed by more episodic moment release, while backprojection identifies two dominant episodes of coherent high-frequency radiation at 0–15 s and 40–60 s (Fig. 3). These complementary observations reveal pronounced changes in rupture propagation and seismic radiation, particularly near 67.3°W, where the high-frequency radiators coincide with the cataloged M_w 7.5 centroid. A simple kinematic test supports a slowdown after ~40 s: propagating the finite-fault slip model at one or two constant rupture speeds places the main moment-rate peak at 30 to 32 s, whereas rupture speeds following the EKI-MultiCMT and backprojection estimates delay the peak to ~36 s and produce a low moment rate between ~40 and 50 s (Fig. S16). The combined low- and high-frequency observations therefore support a single, continuously propagating earthquake with distinct stages of moment release, rupture migration, and seismic radiation, rather than two independent events.

Dynamic controls on rupture speed and episodic radiation

To identify the physical mechanisms controlling the multistage rupture, we use large-scale three-dimensional dynamic rupture simulations to investigate the effects of fault geometry, regional

tectonic stress, and prestress and frictional heterogeneity. These simulations couple nonlinear fault friction, seismic-wave propagation, and off-fault inelastic deformation, allowing spontaneous rupture propagation and arrest [35, 36].

We construct the dynamic rupture model using the mapped Boconó–San Sebastián fault geometry, a 1D velocity model, and regional tectonic stress observations. We prescribe linear slip-weakening friction and a transpressional strike-slip stress field with the maximum horizontal compressive stress, S_{Hmax}, rotating from 130° in the west to 145° in the east (Fig. 1). We additionally introduce prestress heterogeneity informed by the finite-fault slip model and frictional heterogeneity through along-strike variations in the slip-weakening distance D_c [e.g., 16, 21, 37, 38]. We used Ensemble Kalman Inversion (EKI-DR) to estimate the regional relative prestress ratio R_0 (maximum possible stress drop over frictional strength drop; Eq.S9, [13]) and the contribution of data-informed prestress heterogeneity, controlled by a scaling factor α, constrained by geodetic observations and moment-rate history [39] (Methods, Eq. S11).

Regional tectonic stress and fault geometry favor rupture propagation across the Boconó–San Sebastián bend but cannot alone reproduce the observed multistage rupture evolution. To isolate these effects, we first test a regional tectonic-stress model without additional frictional or stress heterogeneity. Despite a uniform regional relative prestress R_0, variations in fault orientation relative to the regional stress increase the resolved on-fault relative prestress ratio from ~ 0.2 along the Boconó Fault to ~ 0.4 near the Boconó–San Sebastián transition, promoting rupture propagation across the bend (Fig S19). Similar geometric and tectonic controls have been identified in other continental earthquakes [17, 18, 21, 40, 41]. However, this model fails to reproduce the geodetically observed surface displacements (55.3% variance reduction, Table S5), moment-rate history, and along-strike variations in slip amplitude, indicating that additional heterogeneity is required.

Introducing prestress and frictional heterogeneity enables the preferred dynamic rupture model to reproduce the coseismic slip and broad multistage rupture evolution (Fig. 4). The EKI-DR inversion identifies an important contribution from pre-stress heterogeneity, with a heterogeneity scaling factor α of 1.1 (Fig. S17, Methods). The preferred rupture model has a moment magnitude of M_w7.57 and fits the geodetic observations with 81.0% variance reduction and a root-mean-square error of 0.10 m (Fig. S20). It dynamically produces the major asperities comparable to the finite-fault model, with peak slip of 2.6 m in the central asperity (Fig. S18). The simulated moment-rate

function captures the broad two-stage moment-release history, including the later peak near 60 s, with an overall rupture duration of ~ 70 s. However, its first major peak occurs at ~31 s, about 10 s earlier than in EKI-MultiCMT and the USGS-Finite fault model, and it overpredicts moment release between 20 and 35 s (Fig. 4F). This mismatch and the absence of a clear slip minimum between the first and the central asperity (Fig. 4A) likely reflect earlier and more concentrated moment release associated with elevated prestress west of the fault bend. Accumulated fault slip remains relatively modest, mostly 1–2 m over a rupture length of nearly 220 km and a down-dip width of 25–30 km, corresponding to an average stress drop of ~ 1.6 MPa.

The preferred simulation reproduces the pronounced rupture speed variations inferred from the seismic observations (Fig. 4 and Fig. 5). During the first ~20 s, the rupture propagates eastward at subshear speed and develops into a broad slip pulse with relatively long rise times (Fig. 5D). It then accelerates to a transient supershear speed between ~20 and 32 s, with V_r/V_s reaching up to $\approx$ 1.05 (Fig. 5C). After ~35–40 s, the rupture decelerates abruptly near a low-prestress barrier at 67.2°W, between two major asperities along the San Sebastián fault.

Stress barriers can slow, arrest, or delay a rupture depending on their strength and spatial extent [42]. In our model, interactions with the free surface and fault bend generate a secondary slip pulse that trails the primary rupture front (Fig. 5A, Movie S1). As the primary front approaches the low-stress barrier, the energy release rate drops below the fracture energy [43], causing the front to decelerate and eventually arrest. However, slip behind it continues and stress transferred from the arrested front reloads the barrier, while the trailing secondary pulse continues to approach the barrier. This allows the rupture to overcome the barrier between ~45 and 60 s without a new nucleation. The rupture then re-accelerates into the adjacent asperity beneath Caraballeda (Fig. 4D) before it arrests at the eastern end of the modeled fault, where we taper the regional prestress. This renewed propagation east of the barrier releases ~26% of the seismic moment in the preferred model, beneath Playa Grande and Caraballeda.

Whether a rupture crosses such a barrier depends on the stress deficit of the barrier relative to the stress drop of the asperities rather than on the length already ruptured, because the energy release rate of a rupture much longer than the seismogenic width saturates [44], and the barrier is ~30 km long, which is comparable to the seismogenic width. In a model with lower regional prestress, $R_0 = 0.20$ instead of $R_0 = 0.33$ (with $\alpha = 1.2$), both the primary front and the trailing

slip pulse are arrested at the barrier, and the earthquake terminates at a magnitude of $M_w \sim 7.47$ (Fig. S23).

The reduced coseismic slip (and, by inference, pre-stress) between the central and eastern asperities (67-67.3°W, see Fig. 2A-C) appears to correlate with the estimated extent of the 1967 M_w 6.6 Caracas earthquake (Fig. 6) [9, 25, 45]. Assuming no creep above the locking depth, ~16-17 mm/yr of fault-parallel motion [23] has accumulated a slip deficit of ~1 m on the segment that ruptured in 1967, compared with ~2 m on the Caraballeda segment that likely ruptured in 1900 [9], consistent with the lower prestress of the barrier relative to the asperities in the preferred model (Fig. 4D). For a locking depth of ~15 km [9], the slip-deficit contrast of ~1 m corresponds to a shear-stress contrast of ~0.7 MPa ($\Delta\tau \approx \mu\,\Delta d/\pi D$ with $\mu = 30$ GPa), or a relative prestress ratio contrast of ~0.15 for the 4.56 MPa strength drop of our model, comparable to that between the barrier and the asperities in the preferred model (Fig. 4D). Historical ruptures may therefore have contributed to the inherited stress heterogeneity that impeded the 2026 rupture.

It is worth noting that the down-dip extent of the 2026 rupture (up to 30-35 km, Fig. 2D) significantly exceeds the fault locking depth inferred from geodetic measurements of interseismic deformation (< 15 km) [9, 23]. The unusually deep penetration of coseismic slip is independently suggested by the USGS moment centroid (depth of 23.5 km, Fig. 2D), depth distribution of aftershocks (Fig. S1), and an agreement between seismic and geodetic moment magnitudes (M_w 7.6). Rupture propagation below the nominal locking depth might result from a strong dynamic weakening [46–48].

The transient supershear phase is favored by inferred rupture migration but is not uniquely required by the observations. In the preferred model, supershear rupture is confined to the central asperity between about 70 and 105 km along strike (Fig. 4B), where the initial on-fault relative prestress ratio reaches $R \approx 0.5$–0.6 (Fig. 4D), above the value of $R \approx 0.46$ ($S \approx 1.19$) required for a supershear transition in three dimensions [49]. A model with high relative prestress produces more persistent supershear propagation, reaching $V_r/V_s > \sqrt{2}$, but overpredicts the observed moment-rate peak by more than a factor of two (Fig. S21, Methods). Conversely, a model with uniform D_c fits the geodetic and moment-rate observations equally well and reproduces the slowdown at the same barrier, while remaining subshear throughout the rupture (Fig. S22, Methods). We prefer the heterogeneous-D_c model because its rupture-speed evolution better agrees with the

apparent acceleration inferred from EKI-MultiCMT and backprojection (Fig. 3E). The kinematic observations therefore permit, but do not require, transient supershear propagation. Consistent with this interpretation, only 8% of aftershocks occurred within the modeled supershear segment (60–100 km along strike), compared with 58% in the easternmost rupture region (Fig. 1), although this contrast does not independently indicate supershear rupture [50].

The dynamic rupture model also offers an explanation for the contrasting histories of high-frequency radiation and moment release. EKI-MultiCMT and the finite-fault model indicate sustained moment release, whereas backprojection reveals concentrated high-frequency radiation associated with abrupt rupture-speed changes and slip-pulse interactions (Fig. 5). Rupture irregularities, including abrupt acceleration and deceleration, variations in local slip duration (rise time), and interactions between rupture fronts, can enhance high-frequency radiation without corresponding peaks in total moment release [38, 51–53]. The observed 40–60 s radiation burst coincides with the modeled primary-front deceleration, secondary-pulse propagation, and rapid shortening of slip duration, suggesting that the apparent doublet reflects a transition in rupture dynamics rather than two independent earthquakes.

Implications for rapid source characterization and seismic hazard

Complex multistage ruptures challenge conventional source characterization, because distinct episodes of seismic radiation can be misidentified as separate earthquakes, potentially misrepresenting rupture length, duration, and directivity. Integrating complementary seismic and geodetic observations with physics-based dynamic rupture simulations provides a framework for linking rupture evolution to physical mechanisms and ground-motion characteristics. Our preferred simulation predicts strongly asymmetric shaking concentrated along and south of the San Sebastián Fault, with near-fault peak ground velocities exceeding 1 m/s (Fig. 4H).

Our simulations use linear slip-weakening friction, a one-dimensional velocity structure, and a simplified fault geometry, without accounting for time-dependent healing, bi-material effects, or small-scale fault complexity. Frictional healing would increase the stress required to break the barrier, such that our modeled delay may represent a lower bound. In addition, a bimaterial contrast across the fault, potentially coupled with fault normal stress and pore-pressure changes, would favor

eastward pulse-like rupture [54–56].

The rupture behavior observed in Venezuela has broader implications for continental strike-slip fault systems, including the San Andreas Fault in California, the North Anatolian Fault in Türkiye [10], the Median Tectonic Line in Japan, and the Enriquillo–Plantain Garden fault system in Haiti [57]. Our results suggest that fault geometry and stress heterogeneity, possibly inherited from historical earthquakes, jointly influence present-day rupture dynamics, while regional tectonic stress and dynamic stress transfer can promote rupture propagation across otherwise restrictive barriers. Understanding these interactions is essential for assessing whether ruptures remain confined to individual segments or propagate across entire fault systems, with important implications for the maximum earthquake size and spatial extent of damaging ground motion.

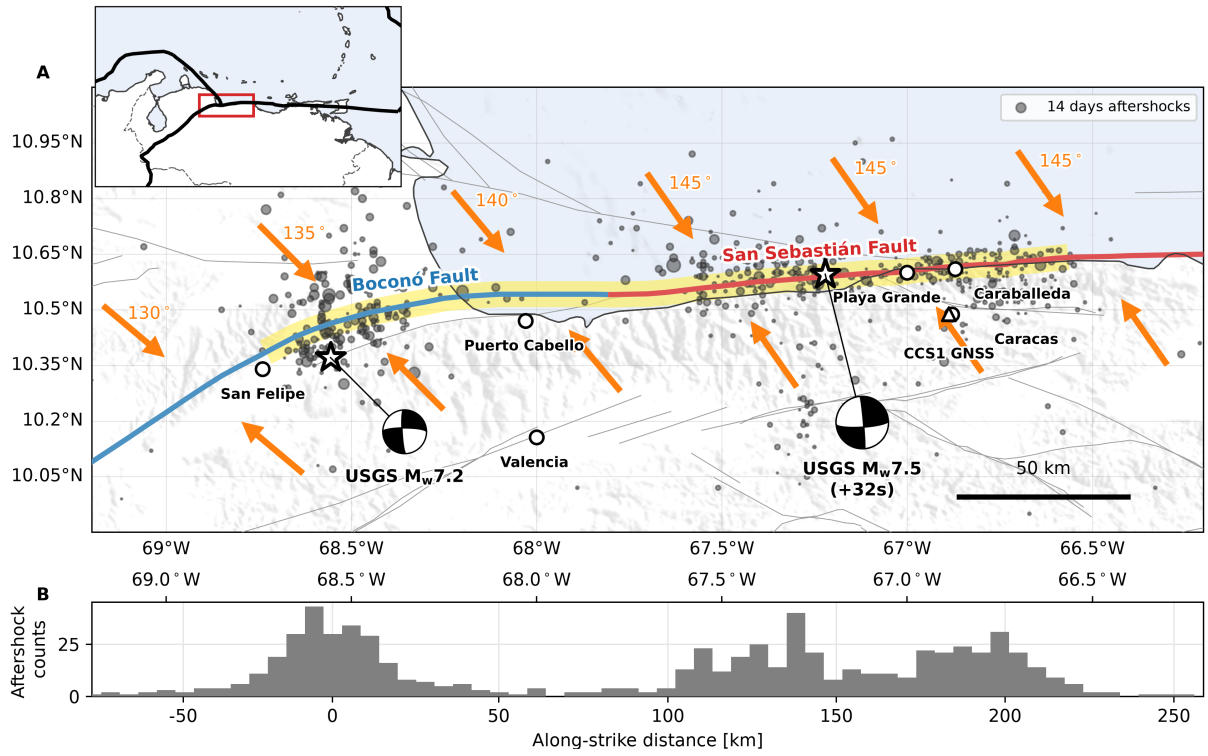


Figure 1: **Tectonic setting and rupture region of the 2026 M_w 7.6 Venezuela earthquake** (**A**) Map of northern Venezuela showing the Boconó Fault (blue), San Sebastián Fault (red), and mapped regional faults (grey). The yellow band marks the inferred rupture region of the 2026 earthquake, and gray circles, sized by magnitude, show aftershocks within 14 days of the mainshock with magnitude $M_L \geq 2.0$. Two stars indicate the epicenters of the two events initially cataloged by the US Geological Survey (USGS) as M_w 7.2 and M_w 7.5, which occurred on 2026-06-24 22:04:31.8 (UTC) and 2026-06-24 22:05:04.1 (UTC), respectively. The orange arrows indicate the $SH_{\max}$ orientation along the fault system. The $SH_{\max}$ rotates clockwise gradually from Boconó Fault to San Sebastián Fault [24]. Open circles indicate the major cities, and a triangle indicates the CCS1 GNSS station. Grey lines indicate the active fault trace in the region [58]. The inset shows the regional tectonic setting along the southern Caribbean plate boundary in thick black lines. The red box indicates the extent of the main map. (**B**) The along-strike aftershock histogram shows depleted aftershocks between 20 and 100 km along-strike distance (68.3°W – 67.6°W).

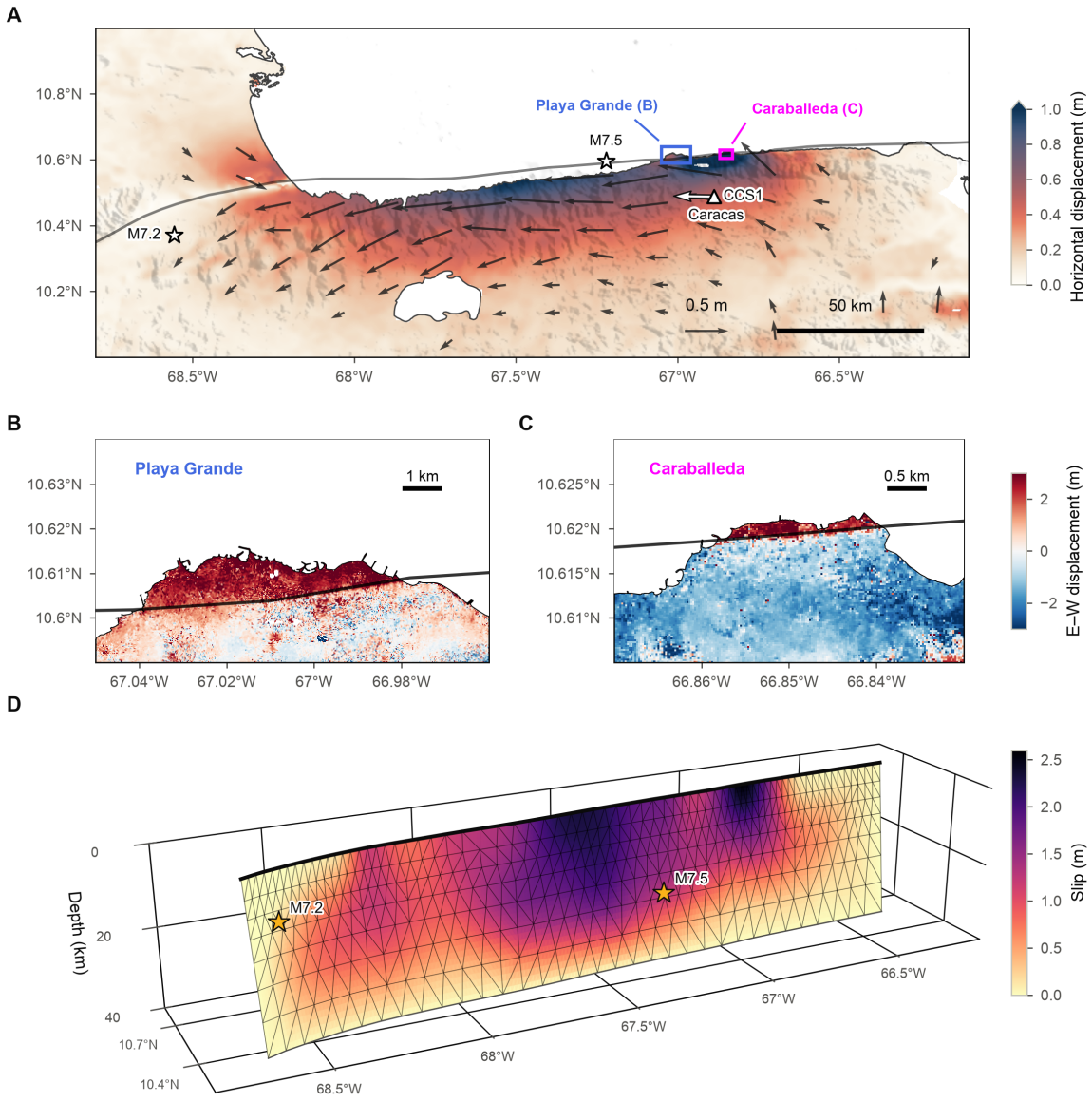
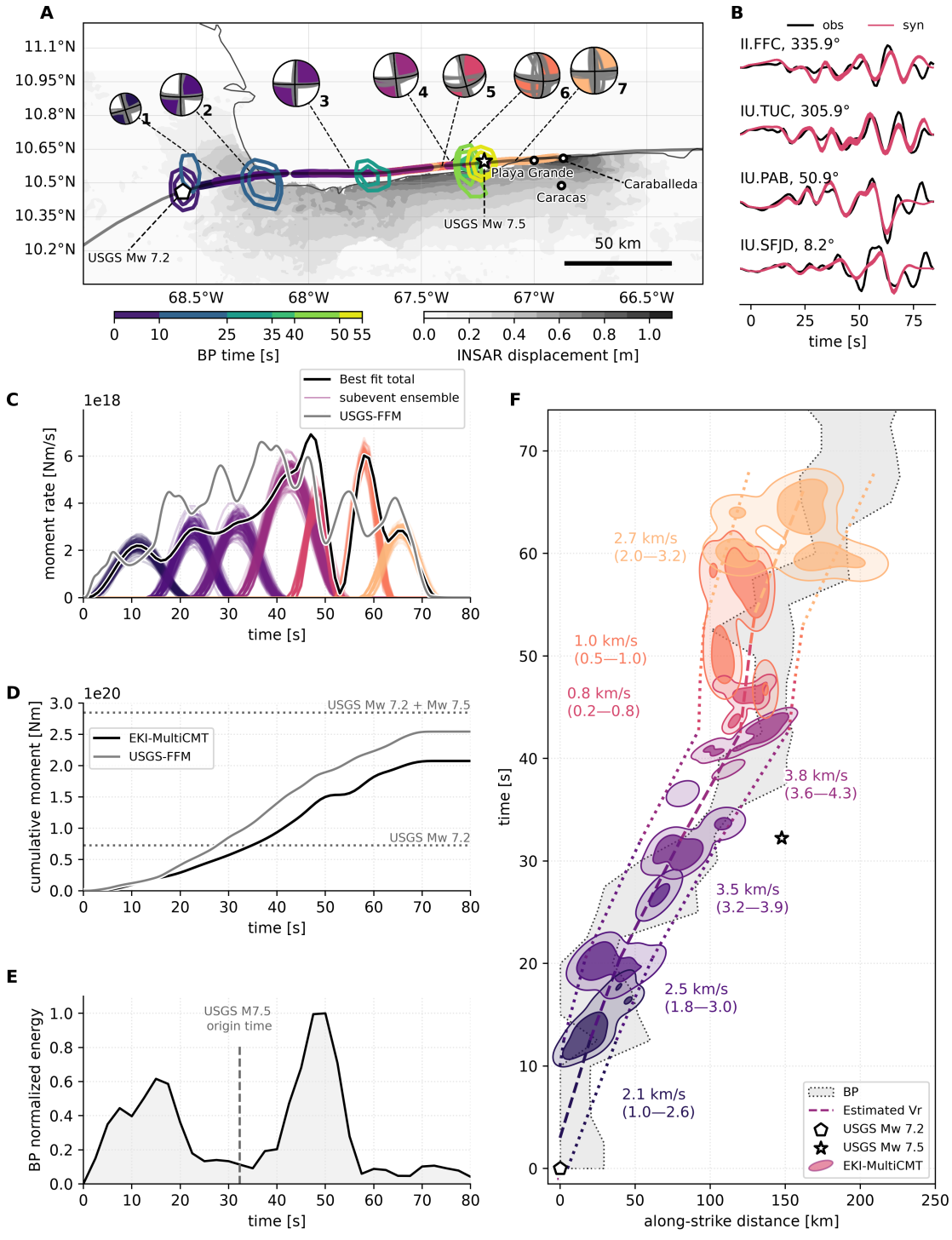


Figure 2: **Coseismic deformation, fault trace, and finite-fault slip distribution** (**A**) Coseismic displacements derived from NISAR and ALOS-2 InSAR observations. Color denotes the magnitude and black arrows denote the orientation of horizontal displacements. The gray line denotes the rupture trace. Blue and magenta boxes outline the Playa Grande and Caraballeda regions shown in panels **B** and **C**, respectively. White arrow denotes the GNSS coseismic displacements at the continuous cite CCS1 [59]. (**B** and **C**) East-west component of horizontal surface displacements in the Playa Grande and Caraballeda regions. Displacements are obtained from cross-correlation of high-resolution (3 m pixel size) PlanetScope optical imagery. Black line denotes the inferred rupture trace. (**D**) Best-fit coseismic slip model obtained from inversions of InSAR data. The fault geometry is constrained using geologic fault maps, geodetic (InSAR and optical) data and EKI-MultiCMT focal mechanisms. Colors indicate slip amplitude. Yellow stars denote the USGS W-phase moment centroids.

Figure 3: **Kinematic rupture evolution from EKI-MultiCMT and teleseismic backprojection** (**A**) EKI-MultiCMT subevent focal mechanisms and backprojection high-frequency radiators projected onto the coseismic displacement field. Each moment tensor represents the subevents scaled by moment, and gray lines indicate the variability in the resolved fault geometry. The color contours delineate the high-frequency radiation with custom window ranges. The background map shows the InSAR-derived displacement. The pentagon and star markers indicate the USGS doublet locations. The circle markers indicate the major cities. (**B**) Comparison between the synthetic and observed teleseismic P-wave displacement records. The synthetic P waves achieve 82% variance reduction relative to the observations. The P waves are bandpass filtered between 0.01 and 0.2 Hz. Top left labels of each waveform list the corresponding station network, code, and azimuth. Fig. S11–S15 shows all waveform comparison. (**C**) Moment-rate history from the ensemble MultiCMT solutions. The black and colored lines show the total and subevent moment-rate functions, respectively. The gray line shows the moment-rate history from the USGS finite-fault slip model (USGS-FFM). (**D**) Comparison of cumulative moment release with the EKI-MultiCMT solution (black solid line), the USGS finite-fault slip model (gray solid line), and the USGS doublet moment release (dashed horizontal lines). (**E**) Normalized high-frequency backprojection energy with a burst at 48 s. The origin time of the USGS M_w7.5 second event (32 s from the origin time) is indicated by the dashed line. The BP energy is computed using a uniform five-second sliding window. We note that the BP energy is not directly correlated with waveform amplitude. (**F**) Space-time rupture evolution from EKI-MultiCMT subevents and backprojection peak-energy windows. The inner and outer colored shading enclose the 50% and 90% density regions of the EKI-MultiCMT ensemble subevents' centroid time and location samples. The gray shading indicates 80% BP relative energy per sliding 5 s window. The dashed line shows the estimated rupture speed following the EKI-MultiCMT subevents and BP migration patterns. Rupture speeds for each segment are listed in the figure, with the uncertainty range between the fastest and slowest possible rupture-front estimates.


A
11.1°N
10.95°N
10.8°N
10.65°N
10.5°N
10.35°N
10.2°N
68.5°W
68°W
67.5°W
67°W
66.5°W
USGS Mw 7.2
USGS Mw 7.5
Playa Grande
Caracas
Caraballeda
50 km
BP time [s]
INSAR displacement [m]
B
obs
syn
II.FFC, 335.9°
IU.TUC, 305.9°
IU.PAB, 50.9°
IU.SFJD, 8.2°
time [s]
C
1e18
moment rate [Nm/s]
time [s]
Best fit total
subevent ensemble
USGS-FFM
D
1e20
cumulative moment [Nm]
USGS Mw 7.2 + Mw 7.5
USGS Mw 7.2
EKI-MultiCMT
USGS-FFM
time [s]
E
BP normalized energy
USGS M7.5
origin time
time [s]
F
time [s]
along-strike distance [km]
2.7 km/s
(2.0—3.2)
1.0 km/s
(0.5—1.0)
0.8 km/s
(0.2—0.8)
3.8 km/s
(3.6—4.3)
3.5 km/s
(3.2—3.9)
2.5 km/s
(1.8—3.0)
2.1 km/s
(1.0—2.6)
BP
Estimated Vr
USGS Mw 7.2
USGS Mw 7.5
EKI-MultiCMT

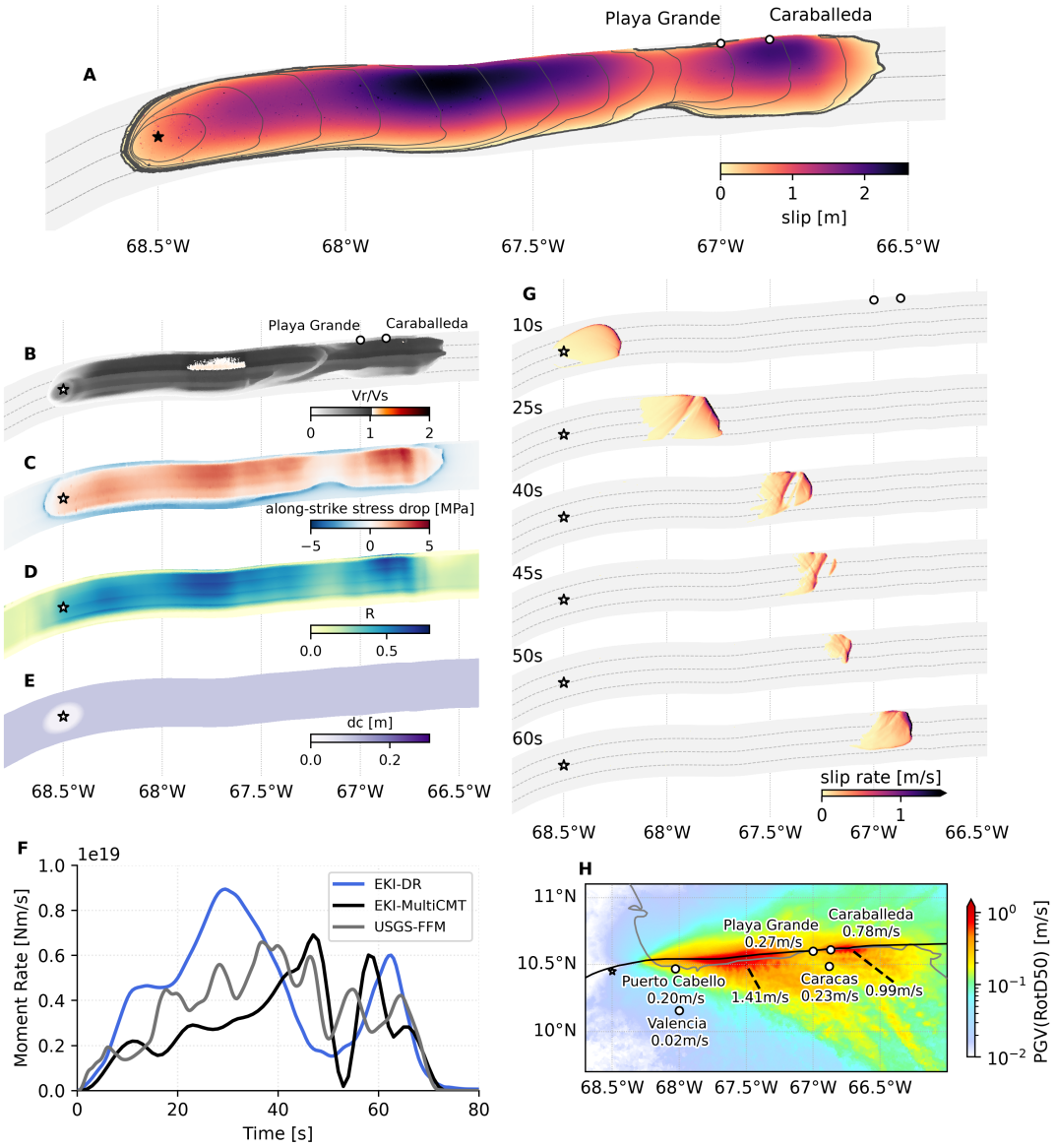


Figure 4: **Preferred dynamic rupture simulation** (**A**) Simulated slip distribution of the Venezuela earthquake. Each black line represents a 5 s rupture time. Heterogeneous distributions of **B–E** simulated rupture speed V_r normalized by the fault-local shear wave velocity V_s, along-strike stress drop, initial relative prestress ratio R, and D_c. Average stress drop over the slip area is 1.62 MPa. **F** Synthetic moment rate release compared with observational inferences from teleseismic data by the USGS model and EKI-MultiCMT. **G** Six snapshots of rupture evolution at 10, 25, 40, 45, 50, and 60 s. Black stars mark the hypocenter, and the dashed line indicates the 10 km depth interval. **H** Peak ground motion distribution. We apply a 2.5 Hz low-pass filter to the simulated data and compute orientation-independent horizontal ground motions without geometric means (RotD50, [60]).

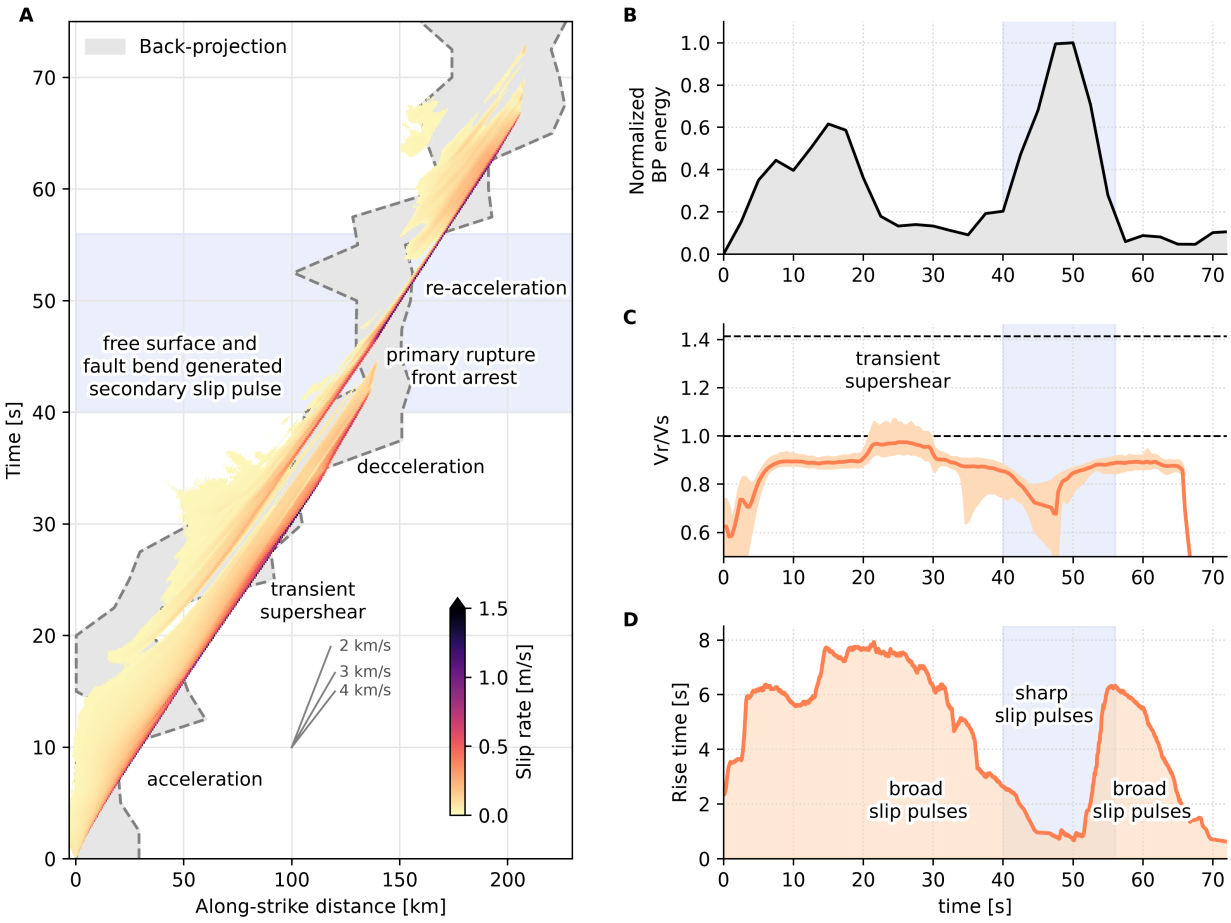


Figure 5: **Comparison between simulated rupture dynamics and observed kinematics.** (**A**) Space-time evolution of the simulated fault slip rate with the back-projection migration. The simulated slip rate is obtained along 15 km depth. The grey shaded area indicates the BP radiators' location. The simulation captures an initial phase of rupture acceleration, a transient supershear episode, subsequent deceleration, and reacceleration. (**B**) Normalized BP energy as a function of time. (**C**) Simulated rupture speed V_r normalized by the fault-local shear wave velocity V_s, with the shaded region indicating variability across the rupture front. Dashed line marks the $V_r/V_s = 1, \sqrt{2}$. The interval with $V_r/V_s > 1$ denotes transient supershear propagation. (**D**) Simulated rise time (local fault slip duration). The rupture varies between long-duration slip and short-duration slip pulses.

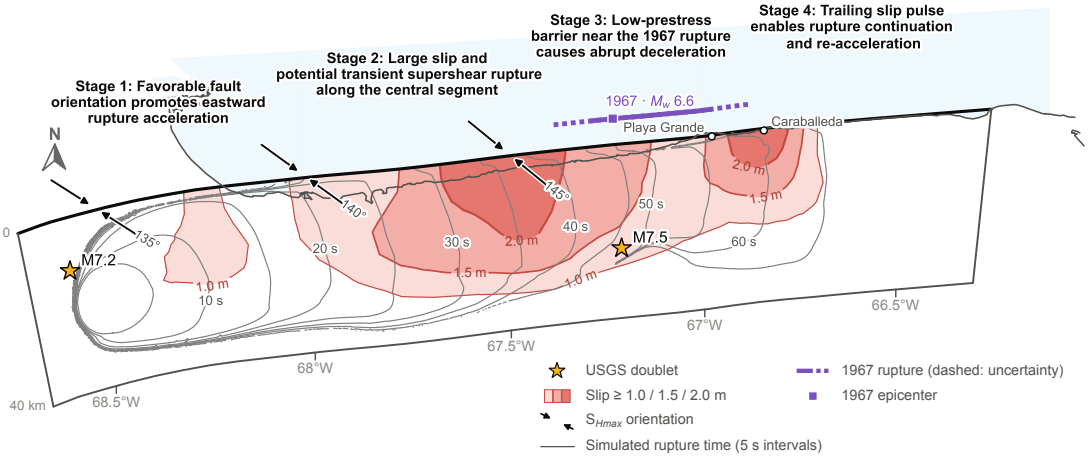


Figure 6: **Schematic diagram of the multi-stage Venezuela earthquake.** Color denotes the amplitude of coseismic slip from the static finite fault model, with increments of 0.5 m. Gray contours denote location of the rupture front from the dynamic rupture model, with increments of 5 s. Other notation is the same as in Figs. 1 and 2. The 1967 earthquake rupture extent is estimated from refs. [45, 61]. The rupture length is uncertain; we assume 35 km based on the length-magnitude scaling for strike-slip earthquakes [3].

Acknowledgments

We thank David Sandwell for the discussions. NISAR data are provided by the National Aeronautics and Space Administration (NASA) via the Alaska Satellite Facility (ASF). ALOS-2 data are provided by the Japanese Space Agency (JAXA) via G-Portal. Copernicus Sentinel-1/2 data are provided by the European Space Agency (ESA). Planet optical data were acquired through the NASA Commercial Satellite Data Acquisition (CSDA) Program.

Funding: This study was supported by the National Science Foundation (NSF, grant nos. EAR-2121568, OAC-2603524, OAC-2311208, OAC-2139536, RISE-2531036 to AAG), by Horizon Europe (grant nos. 101291194, 101093038, 101058129, 101058518 to AAG), the U.S. Geological Survey (award G26AP00141 to AAG), the Statewide California Earthquake Center (SCEC, funded by NSF Cooperative Agreement EAR-2225216 and USGS Cooperative Agreement G26AC00077-00), the Cascadia Region Earthquake Science Center (CRESCENT, funded by NSF Cooperative Agreement EAR-2225286), and Pacific Gas and Electric Company. The authors acknowledge the Texas Advanced Computing Center (TACC) at The University of Texas at Austin for providing computational resources that have contributed to the research results reported within this paper (`http://www.tacc.utexas.edu`). Additional computing resources were provided by the Institute of Geophysics of LMU Munich [62]. We gratefully acknowledge the Gauss Centre for Supercomputing (LRZ, project pn49ha), and the CINECA Supercomputing Centre for providing supercomputing time (Geo-INQUIRE, project no. 101058518).

Author contributions: Conceptualization: J.W.C.W., A.A.G., W.F. Methodology: J.W.C.W., W.F., A.A.G., E.R., Y.F. Investigation: J.W.C.W., A.A.G., W.F., E.R., Y.F. Visualization: J.W.C.W., E.R., Y.F. InSAR data processing: E.R., Y.F. Optical data processing: M.M., Y.M. Fault-trace mapping from InSAR phase gradients: R.G.G., M.Z. Static slip model: E.R., Y.F. Figures: J.W.C.W., E.R., Y.F. Seismic kinematic models: J.W.C.W., W.F., A.A.G. Dynamic rupture models: J.W.C.W., B.W., F.K., A.A.G. Supervision: W.F., Y.F., A.A.G. Writing – original draft: J.W.C.W., A.A.G., E.R., Y.F. Writing – review & editing: all authors.

Competing interests: The authors declare that they have no competing interests.

Data, code and materials availability: The EKI-MultiCMT and EKI-DR codes and the finite-fault slip model, InSAR displacement fields, and optical offsets will be archived on Zenodo before publication. The dynamic rupture simulation setup is available in the Zenodo repository (doi:10.5281/zenodo.23436216). The aftershock data is provided by FUNVISIS. The available code and datasets follow the FAIR data policy [63]. The teleseismic data can be downloaded from the IRIS Wilber 3 system [64]. The GEOFON and USGS catalog events are available online [1, 2].

References

1. Hayes, G. P. The finite, kinematic rupture properties of great-sized earthquakes since 1990. *Earth and Planetary Science Letters* **468,** 94–100. doi:10.1016/j.epsl.2017.04.003 (2017).

2. *GEOFON Data Centre (GFZ Helmholtz Centere for Geosciences)* 1993. https://doi.org/10.14470/TR560404.

3. Thingbaijam, K. K. S., Martin Mai, P. & Goda, K. New Empirical Earthquake Source-Scaling Laws. *Bulletin of the Seismological Society of America* **107,** 2225–2246. doi:10.1785/0120170017. (2024) (2017).

4. Böse, M., Heaton, T. H. & Hauksson, E. Real-time finite fault rupture detector (FinDer) for large earthquakes. *Geophysical Journal International* **191,** 803–812 (2012).

5. Given, D. D. *et al. Technical implementation plan for the ShakeAlert production system: An earthquake early warning system for the west coast of the United States* tech. rep. (US Geological Survey, 2014).

6. Allen, R. M. & Melgar, D. Earthquake early warning: Advances, scientific challenges, and societal needs. *Annual Review of Earth and Planetary Sciences* **47,** 361–388 (2019).

7. Grimm, C., Käser, M., Hainzl, S., Pagani, M. & Küchenhoff, H. Improving earthquake doublet frequency predictions by modified spatial trigger kernels in the epidemic-type aftershock sequence (ETAS) model. *Bulletin of the Seismological Society of America* **112,** 474–493 (2022).

8. Audemard, F. E. & Audemard, F. A. Structure of the Mérida Andes, Venezuela: relations with the South America–Caribbean geodynamic interaction. *Tectonophysics* **345,** 1–26 (2002).

9. Pérez, O. J. *et al.* On the interaction of the North Andes plate with the Caribbean and South American plates in northwestern South America from GPS geodesy and seismic data. *Geophysical Journal International* **214,** 1986–2001. doi:10.1093/gji/ggy230 (2018).

10. Barka, A. & Kadinsky-Cade, K. Strike-slip fault geometry in Turkey and its influence on earthquake activity. *Tectonics* **7,** 663–684 (1988).

11. Wesnousky, S. G. Seismological and structural evolution of strike-slip faults. *Nature* **335,** 340–343 (1988).

12. Harris, R. A., Archuleta, R. J. & Day, S. M. Fault steps and the dynamic rupture process: 2-D numerical simulations of a spontaneously propagating shear fracture. *Geophysical Research Letters* **18,** 893–896 (1991).

13. Aochi, H. The 1999 Izmit, Turkey, Earthquake: Nonplanar Fault Structure, Dynamic Rupture Process, and Strong Ground Motion. *Bulletin of the Seismological Society of America* **93,** 1249–1266. doi:10.1785/0120020167. (2025) (2003).

14. Romanet, P., Sato, D. S. & Ando, R. Curvature, a mechanical link between the geometrical complexities of a fault: Application to bends, kinks and rough faults. *Geophysical Journal International* **223,** 211–232 (2020).

15. Rodriguez Padilla, A. *et al.* The influence of fault geometrical complexity on surface rupture length. *Geophysical Research Letters* **51,** e2024GL109957 (2024).

16. Yao, S. & Yang, H. Rupture phases reveal geometry-related rupture propagation in a natural earthquake. *Science Advances* **11,** eadq0154 (2025).

17. Ando, R. & Kaneko, Y. Dynamic rupture simulation reproduces spontaneous multifault rupture and arrest during the 2016 Mw 7.9 Kaikoura earthquake. *Geophysical Research Letters* **45,** 12–875 (2018).

18. Ulrich, T., Gabriel, A.-A., Ampuero, J.-P. & Xu, W. Dynamic Viability of the 2016 Mw 7.8 Kaikōura Earthquake Cascade on Weak Crustal Faults. *Nature Communications* **10,** 1213. doi:10.1038/s41467-019-09125-w. (2024) (2019).

19. Zhang, Z., Zhang, W. & Chen, X. Dynamic rupture simulations of the 2008 Mw 7.9 Wenchuan earthquake by the curved grid finite-difference method. *Journal of Geophysical Research: Solid Earth* **124,** 10565–10582 (2019).

20. Gabrieli, T. & Tal, Y. Lab earthquakes reveal a wide range of rupture behaviors controlled by fault bends. *Proceedings of the National Academy of Sciences* **122,** e2425471122 (2025).

21. Jia, Z. *et al.* The Complex Dynamics of the 2023 Kahramanmaraş, Turkey, M_{w} 7.8-7.7 Earthquake Doublet. *Science* **381,** 985–990. doi:10.1126/science.adi0685. (2025) (2023).

22. Pérez, O. J. *et al.* Velocity field across the Southern Caribbean Plate Boundary and estimates of Caribbean/South-American Plate Motion using GPS Geodesy 1994–2000. *Geophysical Research Letters* **28,** 2987–2990. doi:10.1029/2001GL013183 (2001).

23. Higgins, M. *et al.* Strain partitioning and interseismic fault behavior along the Caribbean-South American transform plate boundary. *Tectonics* **40,** e2021TC006740 (2021).

24. Castilla, R. *et al.* Present-day stress tensors along the southern Caribbean plate boundary zone from inversion of focal mechanism solutions: A successful trial. *Journal of South American Earth Sciences* **71,** 309–319 (2016).

25. Choy, J. E., Palme, C., Guada, C., Morandi, M. & Klarica, S. Macroseismic interpretation of the 1812 earthquakes in Venezuela using intensity uncertainties and a priori fault-strike information. *Bulletin of the Seismological Society of America* **100,** 241–255 (2010).

26. Rosen, P. *et al.* Synthetic aperture radar interferometry. *Proc. of the IEEE* **88,** 333–382 (2000).

27. Fialko, Y., Simons, M. & Agnew, D. The complete (3-D) surface displacement field in the epicentral area of the 1999 M_w7.1 Hector Mine earthquake, southern California, from space geodetic observations. *Geophys. Res. Lett.* **28,** 3063–3066 (2001).

28. Wright, T., Parsons, B. & Lu, Z. Toward mapping surface deformation in three dimensions using InSAR. *Geophys. Res. Lett.* **31,** L01607 (2004).

29. Zou, X. & Fialko, Y. The 2025 Mw 7.1 Tingri (South Tibet) earthquake: Rupture of normal conjugate optimally oriented faults, shallow coseismic slip deficit, and early afterslip. *Seismol. Res. Lett.* **97,** 1667–1680 (2026).

30. Ulrich, T. *et al.* On predictability of slip, rupture geometry, and speed of the 2025 M 7.8 Mandalay, Myanmar, earthquake. *Nature Communications* **17,** 10173 (2026).

31. Wong, J. W. C., Fan, W., Gabriel, A.-A. & Morzfeld, M. *Multi-CMT Inversion of Complex Earthquakes by Ensemble Kalman Optimization* 2026. doi:10.22541/essoar.15007322/v1. (2026).

32. Fan, W. & Shearer, P. M. Detailed rupture imaging of the 25 April 2015 Nepal earthquake using teleseismic P waves. *Geophysical Research Letters* **42,** 5744–5752 (2015).

33. Ishii, M., Shearer, P. M., Houston, H. & Vidale, J. E. Extent, duration and speed of the 2004 Sumatra–Andaman earthquake imaged by the Hi-Net array. *Nature* **435,** 933–936 (2005).

34. Okuwaki, R., Yagi, Y. & Hirano, S. Relationship between high-frequency radiation and asperity ruptures, revealed by hybrid back-projection with a non-planar fault model. *Scientific reports* **4,** 7120 (2014).

35. Andrews, D. Rupture propagation with finite stress in antiplane strain. *Journal of Geophysical Research* **81,** 3575–3582 (1976).

36. Harris, R. A. *et al.* A Suite of Exercises for Verifying Dynamic Earthquake Rupture Codes. *Seismological Research Letters* **89,** 1146–1162. doi:10.1785/0220170222 (2018).

37. Tinti, E. *et al.* Constraining families of dynamic models using geological, geodetic and strong ground motion data: The Mw 6.5, October 30th, 2016, Norcia earthquake, Italy. *Earth and Planetary Science Letters* **576.** doi:10.1016/j.epsl.2021.117237 (2021).

38. Wong, J. W. C., Gabriel, A.-A. & Fan, W. Dynamic restrengthening and fault heterogeneity explain megathrust earthquake complexity. *Nature Communications.* doi:doi:10.1038/s41467-026-71722-3 (2026).

39. Wong, J. W. C., Gabriel, A.-A. & Fan, W. *Evaluating Dynamic Viability of Finite-Fault Slip Models with Ensemble Kalman Inversion* Preprint. 2026. https://eartharxiv.org/repository/view/15466/.

40. Wollherr, S., Gabriel, A.-A. & Mai, P. M. Landers 1992 “reloaded”: Integrative dynamic earthquake rupture modeling. *Journal of Geophysical Research: Solid Earth* **124,** 6666–6702 (2019).

41. Bustos, J. *et al.* Ground-Motion Intensity in Caraballeda During the 24 June 2026 M w 7.5 Venezuela Earthquake Estimated from CCTV Video. *The Seismic Record* **6,** 411–422 (2026).

42. Paglialunga, F., Ampuero, J. P. & Passelègue, F. Stress Barriers and Their Impact on Rupture Propagation. *Journal of Geophysical Research: Solid Earth* **131,** e2025JB032879. doi:10.1029/2025JB032879. (2026) (2026).

43. Kammer, D. S. *et al.* Earthquake energy dissipation in a fracture mechanics framework. *Nature communications* **15,** 4736 (2024).

44. Weng, H. & Ampuero, J.-P. The dynamics of elongated earthquake ruptures. *Journal of Geophysical Research: Solid Earth* **124,** 8584–8610. doi:10.1029/2019JB017684 (2019).

45. Suárez, G. & Nábělek, J. The 1967 Caracas Earthquake: Fault Geometry, Direction of Rupture Propagation and Seismotectonic Implications. *Journal of Geophysical Research: Solid Earth* **95,** 17459–17474. doi:10.1029/JB095iB11p17459. (2026) (1990).

46. Di Toro, G. *et al.* Fault lubrication during earthquakes. *Nature* **471,** 494–498 (2011).

47. Brown, K. M. & Fialko, Y. ”Melt welt” mechanism of extreme weakening of gabbro at seismic slip rates. *Nature* **488,** 638–641 (2012).

48. Noda, H. & Lapusta, N. Stable creeping fault segments can become destructive as a result of dynamic weakening. *Nature* **493,** 518–521 (2013).

49. Dunham, E. M. Conditions governing the occurrence of supershear ruptures under slip-weakening friction. *Journal of Geophysical Research: Solid Earth* **112,** B07302. doi:10.1029/2006JB004717 (2007).

50. Bouchon, M. & Karabulut, H. The aftershock signature of supershear earthquakes. *science* **320,** 1323–1325 (2008).

51. Madariaga, R. High-frequency radiation from crack (stress drop) models of earthquake faulting. *Geophysical Journal International* **51,** 625–651 (1977).

52. Madariaga, R. High frequency radiation from dynamic earthquake. *Ann. Geophys* **1,** 17 (1983).

53. Li, B. *et al.* Rupture heterogeneity and directivity effects in back-projection analysis. *Journal of Geophysical Research: Solid Earth* **127,** e2021JB022663 (2022).

54. Xia, K., Rosakis, A. J., Kanamori, H. & Rice, J. R. Laboratory earthquakes along inhomogeneous faults: Directionality and supershear. *Science* **308,** 681–684. doi:10.1126/science.1108193 (2005).

55. Dunham, E. M. & Rice, J. R. Earthquake slip between dissimilar poroelastic materials. *Journal of Geophysical Research: Solid Earth* **113,** B09304. doi:10.1029/2007JB005405 (2008).

56. Shlomai, H. & Fineberg, J. The structure of slip-pulses and supershear ruptures driving slip in bimaterial friction. *Nature Communications* **7,** 11787. doi:10.1038/ncomms11787 (2016).

57. Prentice, C. *et al.* Seismic hazard of the Enriquillo–Plantain Garden fault in Haiti inferred from palaeoseismology. *Nature Geoscience* **3,** 789–793 (2010).

58. Styron, R. & Pagani, M. The GEM global active faults database. *Earthquake Spectra* **36,** 160–180 (2020).

59. SIGGMA. *Preliminary GNSS evidence of coseismic deformation in Caracas associated with the 24 June 2026 earthquake* Last accessed: 2026-07-27. 2026. https://siggma.xyz/preliminary-gnss-evidence-earthquake-caracas/.

60. Boore, D. M. Orientation-independent, nongeometric-mean measures of seismic intensity from two horizontal components of motion. *Bulletin of the Seismological Society of America* **100,** 1830–1835 (2010).

61. Rial, J. A. The Caracas, Venezuela, Earthquake of July 1967: A Multiple-source Event. *Journal of Geophysical Research: Solid Earth* **83,** 5405–5414. doi:10.1029/JB083iB11p05405. (2026) (1978).

62. Oeser, J., Bunge, H.-P. & Mohr, M. *Cluster design in the Earth sciences: Tethys* in *High Performance Computing and Communications (HPCC 2006)* **4208** (Springer, 2006), 31–40. doi:10.1007/11847366_4.

63. Li, L., Wong, W. C. J., Schwarz, B. & Lau, T. L. Seismology Perspectives on Integrated, Coordinated, Open, Networked (ICON) Science. *Earth and Space Science* **9,** e2021EA002109. doi:10.1029/2021EA002109. https://doi.org/10.1029/2021EA002109 (2022).

64. Newman, R. *et al. Wilber 3: A Python-Django Web Application For Acquiring Large-scale Event-oriented Seismic Data, Incorporated Research Institutions for Seismology* 2013. https://ds.iris.edu/wilber3/.

Supplementary materials

Materials and Methods

Figs. S1 to S23

Tables S1 to S5

References *(7-0)*

Movie S1

Supplementary Materials for

Fitful but sustained rupture of the 2026 M_w 7.6 Venezuela earthquake

Jeremy Wing Ching Wong[1*,2], Eitan Rapaport Bruck[1], Rubi Garcia Gonzalez[1],Mathilde Marchandon[3], Baoning Wu[1], Fabian Kutschera[1], Molly Zebker[1], Yohai Magen[1], Wenyuan Fan[1], Yuri Fialko[1], Alice-Agnes Gabriel[1,3]1Scripps Institution of Oceanography, University of California San Diego, San Diego, United States of America. [2]Université Côte d'Azur, IRD, CNRS, Observatoire de la Côte d'Azur, Géoazur, Sophia Antipolis, Valbonne, France. [3] Department of Earth and Environmental Sciences, Ludwig-Maximilians-Universität München, Munich, Germany*Corresponding author. Email: jeremywong@ucsd.edu

This PDF file includes:

Materials and Methods

Figs. S1 to S23

Tables S1 to S5

Caption for Movie S1

References

Other Supplementary Materials for this manuscript:

Movie S1

Materials and Methods

InSAR analysis

We use Synthetic Aperture Radar (SAR) data acquired by NISAR and ALOS-2 satellites. Due to dense vegetation cover and surface disruption caused by seismic shaking, the C-band (radar wavelength of 5.6 cm) Sentinel-1 interferograms are strongly decorrelated in the near field (within 10-20 km) of the earthquake rupture. We only use Sentinel-1 pixel offsets to constrain the location of the rupture trace and the amount of surface slip. The L-band (radar wavelength of 24 cm) NISAR and ALOS-2 interferograms remain coherent over much of the study area and provide information about coseismic displacements with 10s of millimeters accuracy and 10s of meters spatial resolution. Table S1 lists interferometric pairs used in this study.

NISAR interferograms are generated from GSLC (geocoded single look complex) products provided by NASA via the Alaska SAR Facility. The ALOS-2 interferograms are generated using GMTSAR software [65] from the Level-1 Single Look Complex (SLC) images provided by the Japan Aerospace Exploration Agency (JAXA). Topographic phase is removed using the Shuttle Radar Topography Mission (SRTM) digital elevation model with 30 m resolution [66]. We process 2 consecutive frames from each track that spans the earthquake rupture. Each ALOS-2 frame consists of 5 sub-swaths that are co-registered, filtered, and merged into a full frame. The merged frames are unwrapped using the branch-cut algorithm [67] for ALOS-2 and the Statistical-cost, Network-flow Algorithm for Phase Unwrapping (SNAPHU) [68] for NISAR. We merge the frames for each track by minimizing phase differences in the overlap areas. Fig. S3 shows the resulting NISAR and ALOS-2 interferograms re-wrapped using the respective radar wavelengths. Most of the interferograms exhibit long-wavelength trends most likely due to ionospheric variations. NISAR interferograms are corrected for the ionospheric phase contributions using ionospheric phase screens provided as part of the GUNW (geocoded unwrapped) data products. Estimates of ionospheric phase screens for the ALOS-2 interferograms are less robust due to a smaller bandwidth of ALOS-2 ScanSAR data. We account for ionospheric contributions to the ALOS-2 and any residual long-wavelength artifacts in the NISAR interferograms by solving for cubic ramps as part of inversions of InSAR data for the coseismic slip distribution, as described in Section “Static finite-fault slip inversion.”

The ALOS-2 interferogram from the ascending track 40 (not shown) spans a time interval of

more than 1.5 years and is more strongly decorrelated compared to the other L-band interferograms that span less than 1 month. Therefore, we don't include the former in our inverse modeling. The remaining data set consists of 4 NISAR interferograms (2 from the ascending tracks 61 and 162, and 2 from the descending tracks 54 and 126), and 3 ALOS-2 interferograms from the descending tracks 133, 134 and 135. Given the right- and left-looking capabilities of the ALOS-2 and NISAR radar instruments, respectively, the available data provide sufficiently diverse lines of sight (LOS) to allow recovery of the full 3-component displacement field. We resample the detrended geocoded interferograms onto a common grid, and for each pixel solve a system of linear equations

$$\mathbf{Au} = \mathbf{d}, \tag{S1}$$

where $\mathbf{u}$ is the displacement vector with the 3 orthogonal East, North, and Up components, $\mathbf{A}$ is the design matrix composed of components of the local unit look vectors, and $\mathbf{d}$ is the data vector composed of LOS displacements from different interferograms. The look vector at each pixel points from the ground to the satellite position in an Earth-centered, Earth-fixed (ECEF) Cartesian coordinate system. The look vectors are normalized to unit length and transformed into the local east-north-up (ENU) coordinate system. We solve the system S1 provided the two conditions are met: (1) more than two independent observations are available for a given pixel, and (2) a condition number of the design matrix $\mathbf{A}$ is less than a prescribed threshold (we use a threshold of 50 in this study). The first condition ensures that the system is not underdetermined, and the second condition ensures that there is sufficient diversity in the look angles, so that all components of the displacement vector are resolved, and the solution is not highly sensitive to errors in the data [27, 28, 69]. The resulting distribution of horizontal displacements is shown in Fig. 2A. The calculated horizontal displacements exhibit a characteristic "butterfly" pattern expected of strike-slip earthquakes [27, 70]. For comparison, we also show coseismic displacements measured using the continuous Global Navigation Satellite System (GNSS) station CCS1 (white arrow and triangle in Fig. 2A). GNSS data were processed by the Society of Geodetic, Geomatic, and Surveyor Engineers of Venezuela [59]. The GNSS data provide independent measurements of the coseismic displacement in the east, north, and vertical directions. As can be seen in Fig. 2A, the InSAR-derived coseismic displacements are in excellent agreement with the available GNSS data at site CCS1.

Optical pixel correlation

We use PlanetScope optical imagery (PlanetScope Ortho Analytic Scene Product) at 3 m spatial resolution to measure the near-fault displacement field along the eastern part of the rupture, where three sections of the surface fault trace are located onshore. Two pairs of pre- and post-earthquake images, acquired on 21-22 June 2026 and 27 June 2026, respectively, are used. Image pairs are selected to minimize cloud cover and temporal separation from the earthquake (Table S4). We correlate each pre- and post-event pair individually using the phase correlator of the open-source software package COSI-Corr [71, 72] with a multiscale sliding correlation window of 128 to 32 pixels and a measurement step of 8 pixels (24 m). We discarded outliers with displacement amplitudes greater than 15 m and data points with a low signal-to-noise ratio (<0.90). We then detrended the displacement fields by removing a residual ramp from each correlation. Finally, we smoothed the surface displacement fields using the non-local means filter implemented in COSI-Corr [73]. We used a patch size of 4×4 pixels, an area dimension of 21×21 pixels, and a noise parameter value of 0.75 [74].

To constrain the rupture trace location and surface slip amplitude, we complemented the interferometric measurements with pixel offsets derived from NISAR and Sentinel-1 radar amplitude images, as well as Sentinel-2 and PlanetScope optical images S7. Pixel offsets derived from cross-correlation of high-resolution (3 m pixel size) PlanetScope optical images are shown in Fig. 2B,C. The offset maps clearly show step-like displacements, which are used to determine the rupture location and slip amplitude. At the west side of the town of Playa Grande, fault offsets are distributed over a relatively broad zone of several kilometers, indicating buried slip, distributed failure, or some combination of both [70, 75].

Static finite-fault slip inversion

We invert line-of-sight (LOS) coseismic displacements for the subsurface slip distribution using piece-wise linear triangular dislocation elements that ensure a continuous slip distribution [29]. The fault geometry is approximated by a 3D curved surface that follows the surface trace, has a constant dip angle of 80 degrees to the south, and extends from the surface to a depth of 40 km (Fig. 2, **D**). Fig. S1 shows the best-fit finite fault model along with aftershocks recorded by a local

seismic network.

The element size gradually increases from ~4 km at the Earth's surface to ~8 km at the bottom of the fault model (40 km). Element size follows the resolution of the data [76, 77]. Each element is sized to half the width of a Gaussian fitted to the averaging kernel of the corresponding model parameter. The mesh and data sub-sampling were updated iteratively until the mesh converged. Each triangular element is given by a superposition of point sources placed at the centroids of a uniform subdivision of each triangle and weighted by the basis function. The Green's functions for point sources are computed assuming a 1D seismic velocity structure shown in Table S2. We then calculate Green's functions for the vertices of the triangular elements, imposing a slip of unity at the given vertex, and a linear decrease of slip to zero to the other vertices of all adjacent triangular elements [29]. This is similar to a treatment of triangular elements with linear basis functions in the Finite Element Method [78]. Finally, we solve for slip **s** at the nodes (vertices of interconnected triangular elements) of the mesh by forming a linear system of equations $\mathbf{Gs} = \mathbf{d}$, where **G** is the Green's function matrix, and **d** is the data vector consisting of sub-sampled NISAR and ALOS-2 LOS displacements. Vector **s** consists of strike-slip and dip-slip components for each node. The matrix **G** accounts for the projection of the 3-component surface displacement field onto the respective lines of sight. We seek the slip distribution u that minimizes a functional

$$\|\mathbf{W}\,(\mathbf{Gs} + \mathbf{Pc} - \mathbf{d})\|_2^2 + \lambda_e^2\,\|\mathbf{Hs}\|_2^2 + \|\mathbf{Bs}\|_2^2\,, \tag{S2}$$

where $||.||_2$ is the Euclidean (L_2) norm, λ_e^2 is the effective regularization parameter, and **H** is the discrete Laplace–Beltrami operator that penalizes curvature in the slip distribution and serves as a regularization operator to avoid ill-posedness [79]. For any given edge of a triangular element, **H** uses cotangent weights if both opposite angles of the edge are acute and symmetrized mean-value weights otherwise [29, 80]. **Pc** is a polynomial (degree of 3) used to estimate long-wavelength trends (ramps) for each interferogram, solved for jointly with the slip and not regularized [81], **W** is a diagonal weighting for each sample by $1/\sqrt{N}$, where N is the number of samples from the respective interferogram, and **B** implements a soft zero boundary condition for slip at the bottom and side edges of the fault [82].

Since the regularization parameter λ_e depends on the mesh, we express the mesh-independent

regularization strength as the effective rank

$$\rho(\lambda) = \mathrm{tr}(\mathbf{R}_{mm}), \qquad \mathbf{R} = \left(\mathbf{A}^{\mathsf{T}}\mathbf{W}^2\mathbf{A} + \mathbf{\Gamma}\right)^{-1}\mathbf{A}^{\mathsf{T}}\mathbf{W}^2\mathbf{A}, \tag{S3}$$

where $\mathbf{A} = [\,\mathbf{G}\;\;\mathbf{P}\,]$ and

$$\mathbf{\Gamma} = \begin{pmatrix} \lambda_{eff}^2\,\mathbf{H}^{\mathsf{T}}\mathbf{H} + \mathbf{B}^{\mathsf{T}}\mathbf{B} & \mathbf{0} \\ \mathbf{0} & \mathbf{0} \end{pmatrix}. \tag{S4}$$

The regularization is chosen by spatially blocked cross-validation [83]. The data were divided into eight along-strike blocks of about $\sim$ 71 km, each block was predicted from an inversion of the other seven, and the misfit of the held-out predictions was minimized (Fig. S2). The corner of the L-curve corresponds to a model about four times smoother, which both the cross-validation and the recovery tests below disfavor.

Fig. S4 shows the interferograms corrected for the ionosphere (NISAR) and long-wavelength ramps estimated from joint inversions. The corrected interferograms display clear coseismic fringes along the fault, suggesting that the de-trending procedure is robust. This is further demonstrated by reasonable model fits and low residuals (Fig. S5).

We estimate model uncertainty from 100 re-inversions, with the same bounds, of the model prediction plus spatially correlated noise. The noise is drawn from an exponential covariance fitted to each interferogram's far-field residual and scaled to its residual rms. A second contribution is the spread of models across the cross-validation range of effective rank (Fig. S6).

Backprojection

Teleseismic back-projection is routinely used to image the rupture process of large earthquakes and to estimate rupture speed [32]. Here, we employ a time-domain P-wave backprojection method to investigate the rupture evolution of the M_w 7.6 Venezuela earthquake [32–34]. We download vertical-component P-wave velocity records from seismic stations at epicentral distances of 30–95°, totaling 1291 traces, with a sampling rate of 100 Hz. The records are filtered with 0.2–1.0 Hz bands using fourth-order Butterworth filters. We calculate theoretical P-wave arrivals using the IASP91 travel-time model [84]. We exclude stations near the nodal planes of the USGS focal mechanism and align the remaining records using multichannel cross-correlation in a window from -3 to 5 s relative to the theoretical P arrivals. Time shifts of up to 3 s and polarity reversals are allowed

during alignment. Records are subsequently selected based on their correlations with the reference beam and visual inspection. In total, 1,272 records are used in the analysis.

We define a spatial grid of potential sources at the hypocentral depth, with a grid spacing of 5 km. The grid extends from 50 km west to 300 km east of the hypocenter and spans 150 km in the north–south direction. To improve the spatial resolution of the backprojection images, we use fourth-root stacking ($N = 4$), although this nonlinear method does not preserve absolute amplitude information [85, 86]. Prior to stacking, each waveform is normalized by its peak amplitude and inversely weighted by the number of contributing stations within 5°, reducing the biases associated with uneven azimuthal and spatial coverage.

To locate the major coherent radiators, we construct backprojection snapshots using non-overlapping stacking windows of (0–10 s, 10–25 s, 25–35 s, 40–50 s, 50–55 s) and normalize each snapshot to its maximum back-projection power (Fig. 3a). The window boundary is selected empirically to isolate distinct episodes of coherent high-frequency radiation. After ~ 55 s, increasing interference from coda waves reduces waveform coherence and thus increases the uncertainty of the inferred radiator locations.

For higher temporal-resolution analyses in Fig. 3E,F, we instead use uniform, half-overlapping 5 s windows throughout the rupture. For each window, we sum the back-projection power over the entire source grid and normalize the resulting time series to obtain a relative measure of the temporal evolution of high-frequency radiation (Fig. 3E). We use the same 5 s back-projection results to construct the space–time migration image by projecting the locations of the resolved radiators onto along-strike distance from the hypocenter (Fig. 3F).

Ensemble Kalman Multiple Centroid Moment Tensor Inversion

We use Ensemble Kalman Multiple Centroid Moment Tensor Inversion (EKI-MultiCMT) to reconstruct the kinematic rupture history of the 2026 M_w 7.6 Venezuela earthquake [31]. The MultiCMT representation describes an earthquake as a sequence of moment-tensor subevents, each characterized by its location, focal mechanism, seismic moment, centroid time, and moment-rate function [87]. Unlike conventional finite-fault inversions, MultiCMT does not require prescribed fault geometry or rupture velocity. EKI-MultiCMT jointly estimates the subevent parameters using Ensemble Kalman Inversion, a derivative-free optimization method that updates an ensemble through esti-

mated cross-covariances between model parameters and synthetic waveforms [88].

Initial ensemble and observational constraints. We follow the inversion framework of Wong *et al.* [31] and use teleseismic backprojection, satellite geodesy, and regional tectonic information to guide the initial spatial and temporal distribution of the ensemble. The detailed formulation of the EKI-MultiCMT and implementation are listed in [31]. In the following, we discuss the specific datasets, ensemble setup, and the new two-stage inversion developed for this event. Backprojection and NISAR observations indicate rupture over approximately 200–250 km along the Boconó–San Sebastián fault system, with high-frequency radiation migrating at an average apparent speed of 2.8–3.5 km/s over ∼70–80 s. We initialize subevents along this migration pattern with sequential centroid times and approximately 50% overlap between neighboring subevent time windows. These distributions provide initial samples rather than fixed bounds on the inversion parameters. Supplementary Table S3 summarizes the initial parameter distributions. Using satellite observations and the known Boconó-Sebastian fault system, we restrict the ensemble to the identified trace to reduce the inversion dimensionality.

Waveform selection and processing. We select 36 teleseismic stations at epicentral distances of 30°–90° (Fig. S9). Records are selected separately for each waveform type based on signal-to-noise ratio. The joint inversion uses 24 P-wave records, 21 SH-wave records, and 61 surface-wave records. Body-wave displacements are resampled to 1 Hz and surface-wave displacements to 0.1 Hz. We apply bandpass filters of 5–100 s for P waves, 20–100 s for SH waves, and 50–200 s for surface waves. Records are normalized using a common scaling factor for each waveform type, preserving relative amplitudes between stations and radiation-pattern information. We assign relative weights of 4:2:1 to P, SH, and surface waves, respectively, for the second-stage joint inversion. We use Instaseis with the Syngine green's function library PREM *prem_a_2s* to generate the synthetic waveforms [89, 90].

Two-stage inversion strategy. Teleseismic P-wave observations show two distinct phases: relatively low-amplitude signals during the first ∼40 s, followed by signals with more than twice the displacement amplitude between ∼40 and 80 s. To prevent the later, higher-amplitude arrivals from dominating the inversion, we adopt a two-stage strategy. We first invert the initial 40 s of teleseismic P-wave observations to constrain the early rupture. We then incorporate these results into a joint inversion of the full P-, SH-, and surface-wave records to reconstruct the complete

rupture history. The temporal division approximately coincides with the separation of the two events initially reported in the USGS and GEOFON catalogs [1, 2]. This two-stage inversion is similar to the multistage Bayesian inversion used in [91].

Rather than fixing the first four subevents, we impose a prior to preserve the inverted first four-subevent source parameters while allowing adjustments during the joint inversion. We initialize these subevents by perturbing the first-stage estimates with zero-mean Gaussian noise and incorporate their inferred parameters as Tikhonov regularization within the Ensemble Kalman Inversion (TEKI) framework [92]. We estimate the prior variance C_{prior} from the ensemble spread from the first-stage inversion. Hence, the second-stage objective function is

$$\mathcal{J}(\theta) = \frac{1}{2}||\mathbf{G}(\boldsymbol{\theta}) - \mathbf{d}||^2_{\mathbf{R}^{-1}} + \frac{1}{2}||\boldsymbol{\theta}_{1:4} - \boldsymbol{\theta}^*_{1:4}||^2_{\mathbf{C}^{-1}_{\text{prior}}}, \tag{S5}$$

where $\boldsymbol{\theta}^*_{1:4}$ denotes the first-stage reference solution, $\mathbf{C}_{\text{prior}}$ specifies the prior covariance of the first four subevents, and $\mathbf{R}$ is the observational error covariance. The prior covariance controls allowed deviations from the first-stage estimates, enabling the inversion to account for waveform interference and parameter trade-offs between early and later subevents without discarding early-rupture constraints.

First stage: Initial 40 s of teleseismic P waves. We invert the initial 40 s of P-wave observations using models containing one to five subevents. The four-subevent model achieves the highest waveform variance reduction (80.0%) and the lowest BIC (Fig. S10a, Fig S11), and is therefore selected to represent the early rupture.

We assess parameter variability using a Randomized-then-optimization procedure [31, 93–95]. We conduct ten independent inversions with randomized initial ensembles and perturbed observations. Each inversion produces an optimized, data-consistent solution, and the variability among these solutions provides an empirical measure of inversion stability and parameter uncertainty. The ten solutions yield waveform variance reductions of 78.4–82.6%, and Fig. 3F shows the subevent centroid time and location variability in the space-time migration plot.

Second stage: Joint inversion of full teleseismic waveforms. We extend the inversion to the full 90-s P-wave displacement records, together with SH- and surface-wave observations, to reconstruct the complete rupture history. The four subevents inferred from the first stage provide initial estimates of the early rupture, while additional subevents represent subsequent moment

release.

We invert the full-trace waveforms with a total of five to eight subevents. The seven-subevent model achieves the highest waveform variance reduction (83.6%) and the lowest BIC (Fig. S10)b, Fig S12– S15). Similarly, we conduct the Randomized-then-optimization procedure and yield ten sets of ensemble solutions with waveform variance reduction of 77.6–85.1%.

Constructing subsurface fault geometry

To construct the fault geometry of the Boconó and San Sebastián faults, we first digitize the surface trace of the Venezuela earthquake rupture using phase gradients derived from NISAR data, the E-W component of horizontal displacements derived from NISAR data, and optical pixel correlation offset from Sentinel-2 and PlanetLab data. We connect the offshore trace and extend the fault segments beyond the rupture area using the active surface fault trace [58]. To determine the subsurface fault geometry from the surface fault trace, we use the EKI-MultiCMT inversion of subevent focal mechanisms. All subevents have sub-vertical fault plane with dip angles ranging from 70 to 90°, with median dip angles around 80–85 °. Therefore, we construct a constant 80° dipping-angle fault network across the Boconó and San Sebastián faults.

Ensemble Kalman Inversion (EKI) 3D dynamic rupture simulations

We use three-dimensional dynamic rupture simulation to investigate the faulting conditions controlling the rupture dynamics of the Venezuela earthquake. Dynamic rupture simulation solves the governing equations for coupled seismic wave propagation and on-fault frictional evolution and can include off-fault inelastic deformation, allowing spontaneous rupture to emerge from prescribed stress, frictional, and structural conditions [36, 96, 97]. To constrain the heterogeneous prestress conditions, we employ Ensemble Kalman Inversion for Dynamic Rupture simulations (EKI-DR) [39, 88], using geodetic displacements and the seismic moment-rate history as observational constraints.

We perform simulations using SeisSol [98], which solves the elastodynamic equations using the arbitrary high-order derivative discontinuous Galerkin (ADER-DG) method [99, 100]. The fault geometry follows the connected Boconó–San Sebastián fault system constrained by satellite geodesy, EKI-MultiCMT focal mechanisms, and mapped active fault traces [58] (Methods Sec. “Construct-

ing subsurface fault geometry"). The fault dips at 80° and extends from the surface to 40 km depth. We adopt the same one-dimensional layered elastic structure used for the static finite-fault inversion, derived from the regional CRUST2.0 model [101] (Table S2). The computational domain includes topography from the 450-m GEBCO grid [102] and neglects viscoelastic attenuation.

The model domain is discretized into ∼17.0 million tetrahedral elements, with mesh refinement in a 350 km × 100 km high-resolution region aligned with the predominantly east–west fault system to resolve frequencies up to 1 Hz. The characteristic fault on-fault edge length is 250 m, which resolves the process zone (with $D_c = 0.1$ m) with a measured width of 250 m in our simulation using a polynomial basis function of degree $p = 5$ (order 6 accuracy) with local time stepping [103].

Simulations are configured to run for up to 150 s. Each simulation takes 3,500 GPU-hours on the Leonardo HPC cluster, and 58,000 CPU-hours on the Frontera HPC cluster [104].

Fault friction, rupture nucleation and off-fault plasticity. We prescribe linear slip-weakening friction [35, 105], following 3D dynamic rupture model setups of previous large strike-slip earthquakes [17, 21, 30, 106–109]. Fault strength, τ, at any location on the fault is calculated using:

$$\tau_f = -C - \min\left(0, \sigma_n'\right)\left(\mu_s - \frac{\mu_s - \mu_d}{D_c}\min(AS, D_c)\right), \tag{S6}$$

where C is the frictional cohesion, σ_n' is the compressive effective normal stress magnitude, μ_s and μ_d are the static and dynamic friction coefficients, and AS is accumulated fault slip. We prescribe uniform coefficients $\mu_s = 0.6$ and $\mu_d = 0.22$, with cohesion increasing linearly from 0.5 MPa below 6 km depth to 1.5 MPa at the surface.

To reproduce the observed variation in rupture dynamics, we prescribe an along-strike distribution of D_c, linearly interpolated between control points. The D_c ranges from 0.025 to 0.20 m, with lower values over the western and central fault segments and higher values farther east. Specifically, D_c is prescribed as 0.06, 0.10, 0.025, 0.025, 0.20, 0.20, 0.10, and 0.10 m at along-strike coordinates of 0, 60, 70, 100, 110, 150, 160, and 200 km, respectively. Within the nucleation region, D_c is reduced to 0.03 m inside an 8-km radius and transitions linearly to the background distribution between radii of 8 and 12 km.

Rupture is initiated through a smooth forced-nucleation method [36] centered at 20 km depth (68.528°W, 10.436°N), following the hypocenter location of the USGS finite-fault slip model [1].

The prescribed nucleation front expands within an 8-km-radius patch at a nominal speed of $0.7V_s$, with a smooth increase in the forced-rupture time approaching the patch boundary. Beyond this region, rupture propagation evolves spontaneously according to the initial stress and frictional conditions.

We prescribe a depth-dependent effective normal stress assuming depth-dependent high pore-fluid pressure [110]:

$$\sigma_n'(z) = \min[12\ \text{MPa}, 0.34\rho g \max(z, 200\text{m})]$$

where z denotes positive depth, $\rho = 2670$ kg/m^3, and $g = 9.8$ m/s^2. This stress scale increases with depth until reaching a cap of 12 MPa at approximately 1.35 km. The resulting effective normal traction on the fault also depends on the resolved three-dimensional initial stress tensor. The absolute effective stress and friction coefficients are not independently constrained by the rupture observations. Under linear slip weakening, the strength drop, relative prestress, and fracture energy jointly control rupture behavior, while variations in effective normal stress also influence dynamic fault-normal stress perturbations and off-fault yielding.

We assume a depth-dependent, non-associated Drucker-Prager elasto-viscoplastic rheology to model coseismic off-fault plastic deformation [96, 111–113]. We parameterize off-fault plasticity by a bulk internal friction coefficient and 3D variable plastic cohesion. We use a uniform bulk friction coefficient of 0.6, matching our on-fault static friction coefficient, and define the plastic cohesion C_{plastic} to vary linearly with effective confining pressure [96, 112, 114]:

$$C_{\text{plas}}(z) = C_{\text{plas},0} + C_{\text{plas},1}(z)\sigma_c' \,. \tag{S7}$$

We set $C_{\text{plas},0}$ to 1 MPa to represent partially consolidated sediments [115], whereas $C_{\text{plas},1}$ linearly reduces from 1 to 0 at depths shallower than 5 km.

Regional stress and relative prestress ratio We construct the initial stress field by combining an Andersonian strike-slip regional stress tensor [116, 117] and a heterogeneous stress field derived from the finite-fault slip model. The regional stress tensor assumes that the vertical principal stress corresponds to the intermediate principal stress, σ_2, with a stress shape ratio

$$\nu = \frac{\sigma_2 - \sigma_3}{\sigma_1 - \sigma_3} = 0.5, \tag{S8}$$

where $\sigma_1 \geq \sigma_2 \geq \sigma_3$ denote the principal compressive stresses.

To represent the regional variation in tectonic stress orientation, we prescribe a clockwise rotation of the maximum horizontal compressive stress, S_{Hmax}, from 130° in the west to 145° in the east (Fig. 1A) [117, 118]. The orientation varies linearly between local coordinates $x = -50$ and 100 km and remains constant outside this interval.

We parameterize the regional prestress using the relative prestress ratio [13],

$$R = \frac{\tau_0 - \tau_d}{\tau_s - \tau_d} = \frac{\tau_0 - \mu_d \sigma_n'}{(\mu_s - \mu_d)\sigma_n'}, \tag{S9}$$

where τ_0, τ_s, and τ_d are the initial shear traction, static strength, and dynamic strength, respectively. The corresponding seismic strength parameter is

$$S = \frac{\tau_s - \tau_0}{\tau_0 - \tau_d}, \qquad R = \frac{1}{1 + S}. \tag{S10}$$

.

Following [18], the regional prestress level R_0 is specified on an optimally oriented fault. The corresponding principal stress magnitudes are used to construct the three-dimensional Andersonian stress tensor, which is subsequently resolved onto the nonplanar fault geometry. Consequently, the local on-fault prestress ratio R_f depends on both regional stress magnitude and fault orientation and varies significantly even for uniform R_0, and is always equal to or less than R_0.

To introduce additional along-strike prestress heterogeneity, we parameterize the regional stress field using the seismic strength ratio S at discrete along-strike control points, with linear interpolation between them. In the reference configuration, S increases from 1.2 at $x = 0$ km to 1.5 at 40 km and 2.0 at 80 km, remains at 2.0 through 200 km, and increases to 20 at 220 km to promote terminal rupture arrest. The corresponding relative prestress ratios are approximately 0.45, 0.40, and 0.33 over the principal rupture segments.

$$s_{ij}' = \Omega\, b_{ij} + \alpha\, c_{ij} + (1 - \Omega)\, \sigma_{zz}'\, \delta_{ij}, \tag{S11}$$

where b_{ij} denotes the Andersonian stress tensor, c_{ij} is the sign-reversed deviatoric stress change of the finite-fault slip model, $\alpha = 1.1$ is its scaling coefficient, and δ_{ij} is the Kronecker delta.

The depth-dependent modulation function $\Omega(d)$ equals 0.4 at depths shallower than 2 km, increases linearly to one between 2 and 4 km, and remains one between 4 and 30 km. It decreases to 0.5 between 30 and 35 km and remains at 0.5 below 35 km to taper stress at depth. We choose

35 km because it is the downdip limit of the finite-fault slip model. This modulation reduces the regional deviatoric stress outside the seismogenic depth interval.

Ensemble Kalman inversion for dynamic rupture model initial stress conditions

Following our previously developed EKI-DR framework [39], we jointly invert for two parameters controlling the initial stress state: the amplitude scaling α of the finite-fault-model-derived stress perturbation and the regional prestress parameter R_0. Each EKI ensemble member corresponds to a fully spontaneous 3D SeisSol simulation, and the ensemble is iteratively updated using the joint misfit between modeled and observed geodetic displacements and moment-rate functions.

Starting from an ensemble spanning $\alpha = 1.0{-}1.2$ and $S_{\mathrm{reg}} = 2{-}4$, EKI iteratively updates the parameter ensemble using the ensemble-estimated cross-covariance between the model parameters and simulated observables. We perform the iterative inversion until the ensemble converges toward a region of parameter space that provides a joint fit to both the geodetic and moment-rate observations.

We select the preferred model from the best-fitting EKI ensembles (Fig. S17). Among the first updated ensemble, the model with $\alpha = 1.10$ and $R_0 = 0.33$ ($S = 2$) provides the best geodetic variance reduction (81.0%) and a low geodetic residual RMSE (10.29 cm), while its seismic moment, 2.65×10^{20} Nm (M_w=7.59), and rupture duration (68.1 s) are consistent with the target event. We therefore use this model as the preferred dynamic rupture for subsequent analysis.

Ground motion analysis

We compute peak ground velocities from the simulation of the preferred model (polynomial degree 5, with 250 m on-fault mesh resolution), with free-surface output every 0.1 s. At each surface element, we low-pass filter the two horizontal velocity components at 2.5 Hz, rotate them over all azimuths, and take the median of the peak values (RotD50) [60]. The velocity model includes no sediments with shear-wave speeds below 1.95 km/s and no anelastic attenuation, so absolute amplitudes at basin sites are uncertain.

Supplementary Materials

Table S1: Coseismic interferometric pairs used in this study. Letters preceding the track numbers denote ascending (A) and descending (D) tracks, respectively. B_{perp} denotes a perpendicular baseline. Dates of the reference and secondary radar acquisitions are in a ”year/month/day” format.

Mission	Track	Reference	Secondary	B_{perp} (m)
NISAR	A162	2026/06/13	2026/06/25	22
	A061	2026/06/18	2026/06/30	25
	D054	2026/06/17	2026/06/29	17
	D126	2026/06/22	2026/07/04	7
ALOS-2	A040	2025/01/14	2026/06/30	203
	D133	2026/06/19	2026/07/17	71
	D134	2026/06/10	2026/07/08	124
	D135	2026/06/15	2026/06/29	85

Table S2: 1D velocity structure averaged from CRUST2.0 [101].

layer	depth [km]	thickness [km]	V_p [km/s]	V_s [km/s]	rho [g/cm^3]
hard sediments	2.00	2.00	3.75	1.95	2.37
upper crust	10.58	8.58	6.10	3.50	2.75
middle crust	19.25	8.67	6.50	3.65	2.87
lower crust	27.92	8.67	7.00	3.90	3.01
mantle	999	999	8.20	4.70	3.40

Table S3: **Initial ensemble distribution for the EKI-MultiCMT inversion.**

Case	First 40 s inversion	100 s inversion
number of ensemble	100	100
iterations	16	16
data	P (5–100s)	P (5–100s) & SH (10–100s) & surface waves (50–100 s)
Initial ensemble distributions*		
Depth	$U(2-16\text{km})$	$U(2-16\text{km})$
Moment	$\mathcal{D}(U(0.9-1.1)\cdot 1\times 10^{19}\text{Nm})$	$\mathcal{D}(U(0.9-1.1)\cdot 2.5\times 10^{19}\text{Nm})$
Strike	$U(70^\circ-100^\circ)$	$U(70^\circ-100^\circ)$
Dip	$U(70^\circ-90^\circ)$	$U(70^\circ-90^\circ)$
Rake	$U(160^\circ-200^\circ)$	$U(160^\circ-200^\circ)$
Duration	$U(6-16s)$	$U(6-16s)$
Centroid time	50% overlap with total duration of 40 s	50% overlap with total duration of 100 s

* U represents uniform distribution, $\mathcal{D}$ represents Dirichlet partition .

+ The subevent moments are determined by a Dirichlet partition of a uniformly distributed total seismic moment.

Table S4: PlanetScope Imagery meta-data.

Covered area	Product type	Spatial resolution (m)	Acquisition date (year-month-day)	Image ID
Playa Grande	Analytic Ortho Scene	3	26-06-22	20260622_153256_45_253b
	Analytic Ortho Scene	3	26-06-27	20260627_153104_40_2530
Caraballeda	Analytic Ortho Scene	3	26-06-21	20260621_145736_82_2558
& Naiguata	Analytic Ortho Scene	3	26-06-27	20260627_145723_40_2553

Table S5: List of alternative dynamic rupture models with corresponding figures and geodetic variance reduction.

Model	Figures	Geodetic variance reduction
Uniform Regional relative prestress model $(R_0, \alpha) = (0.67, 0)$	Fig. S19	55.3%
Uniform D_c model with $(R_0, \alpha) = (0.33, 1.1)$	Fig. S22	81.5%
Persistent supershear model with $(R_0, \alpha) = (0.33, 1.2)$	Fig. S21	79.0%
Barrier-arrest model with $(R_0, \alpha) = (0.2, 1.2)$	Fig. S23	43.0%

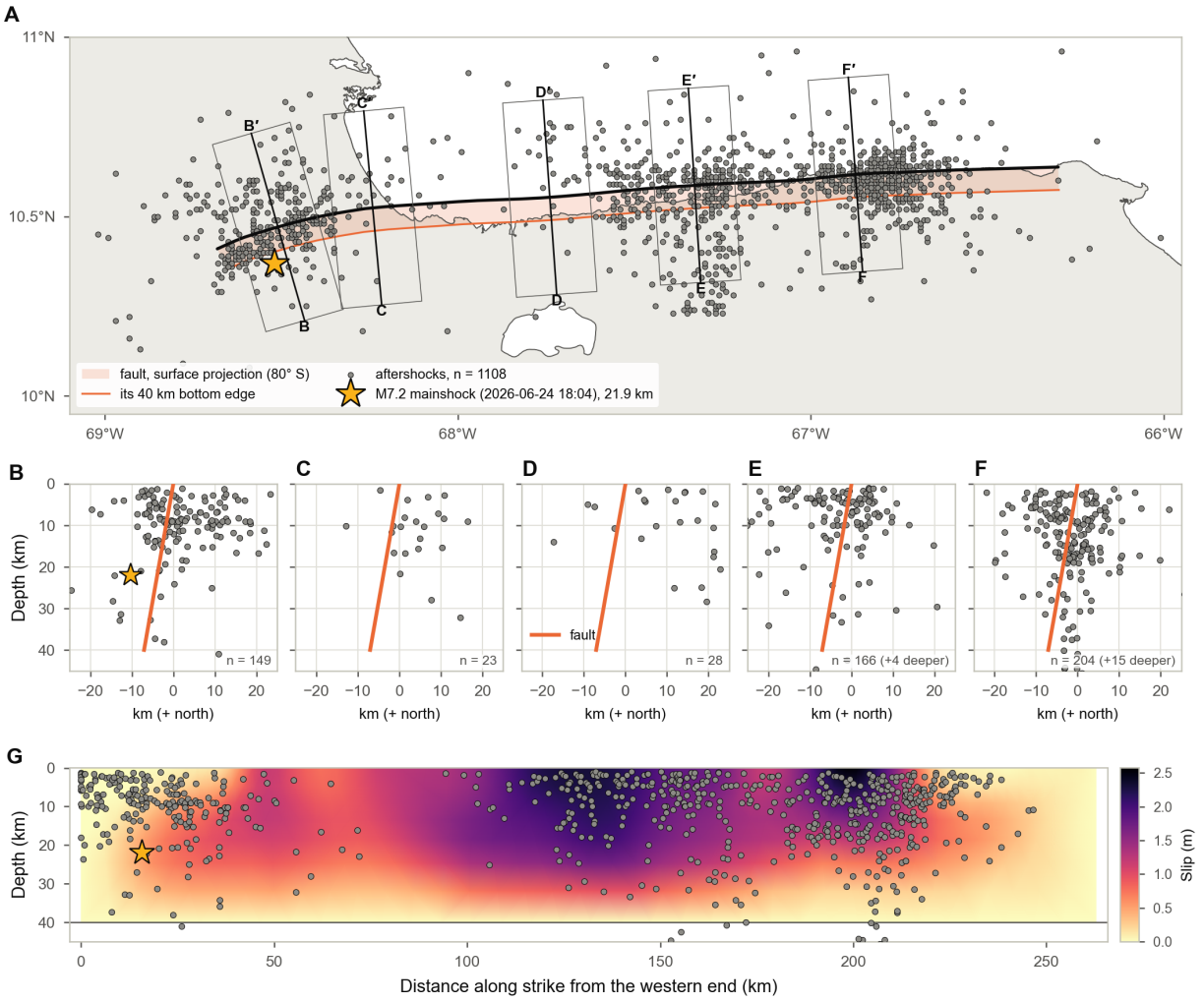


Figure S1: A) A map view of aftershocks located within 40 km of the earthquake rupture. Aftershock epicenters are denoted by gray circles. B) A distribution of aftershocks located within 15 km from the rupture trace in several cross-sections shown in panel A. Red lines denote the reference fault model.

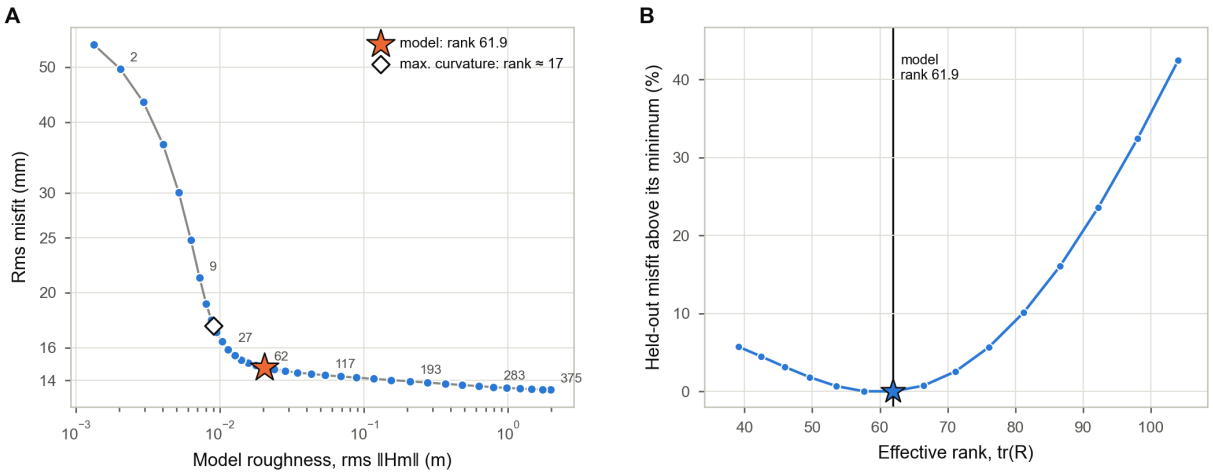


Figure S2: a) L-curve showing misfit versus model roughness. b) Blocked cross-validation curve and minimum.

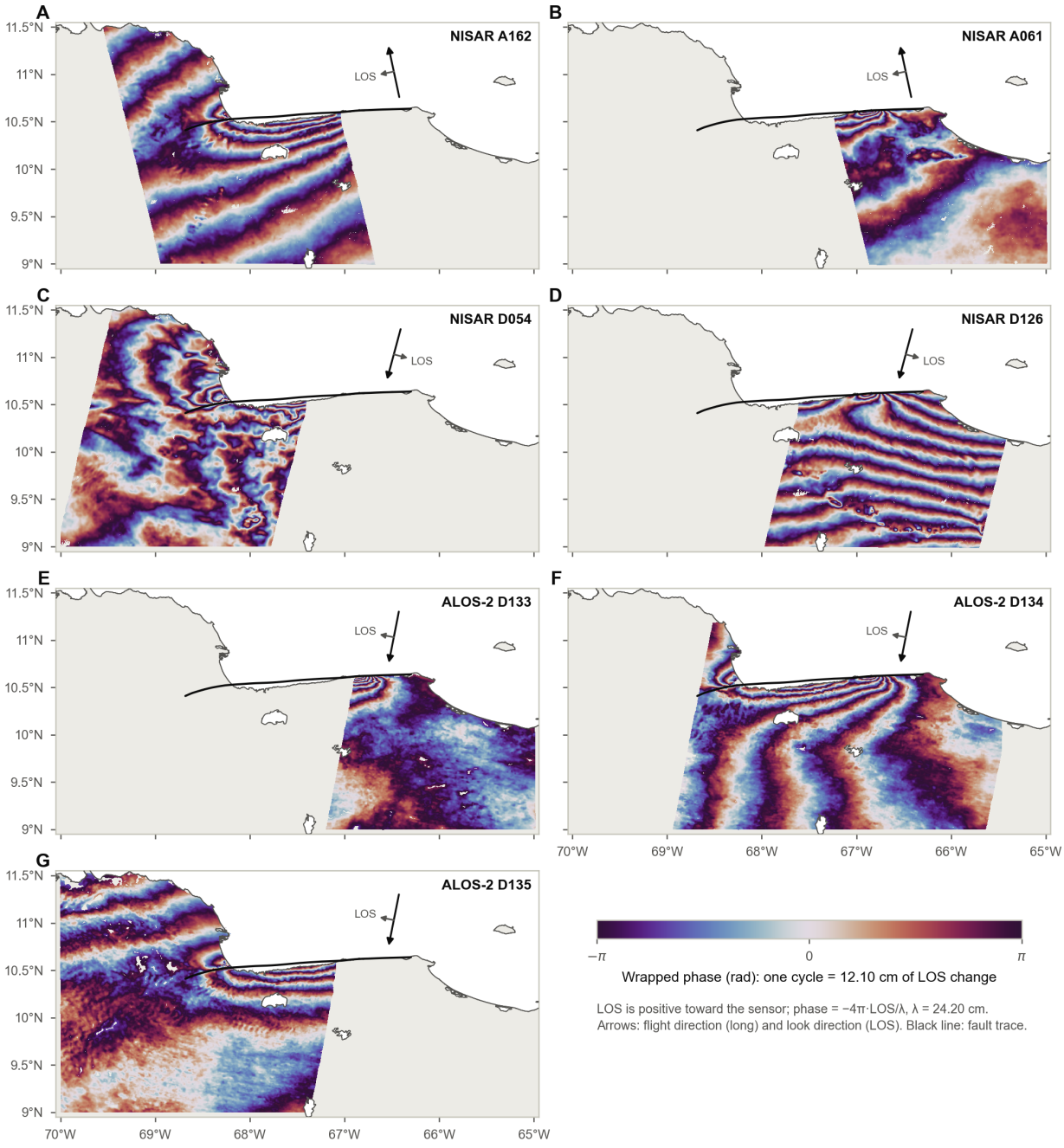


Figure S3: Original NISAR and ALOS-2 interferograms. Color denotes filtered wrapped radar phase, in radians.

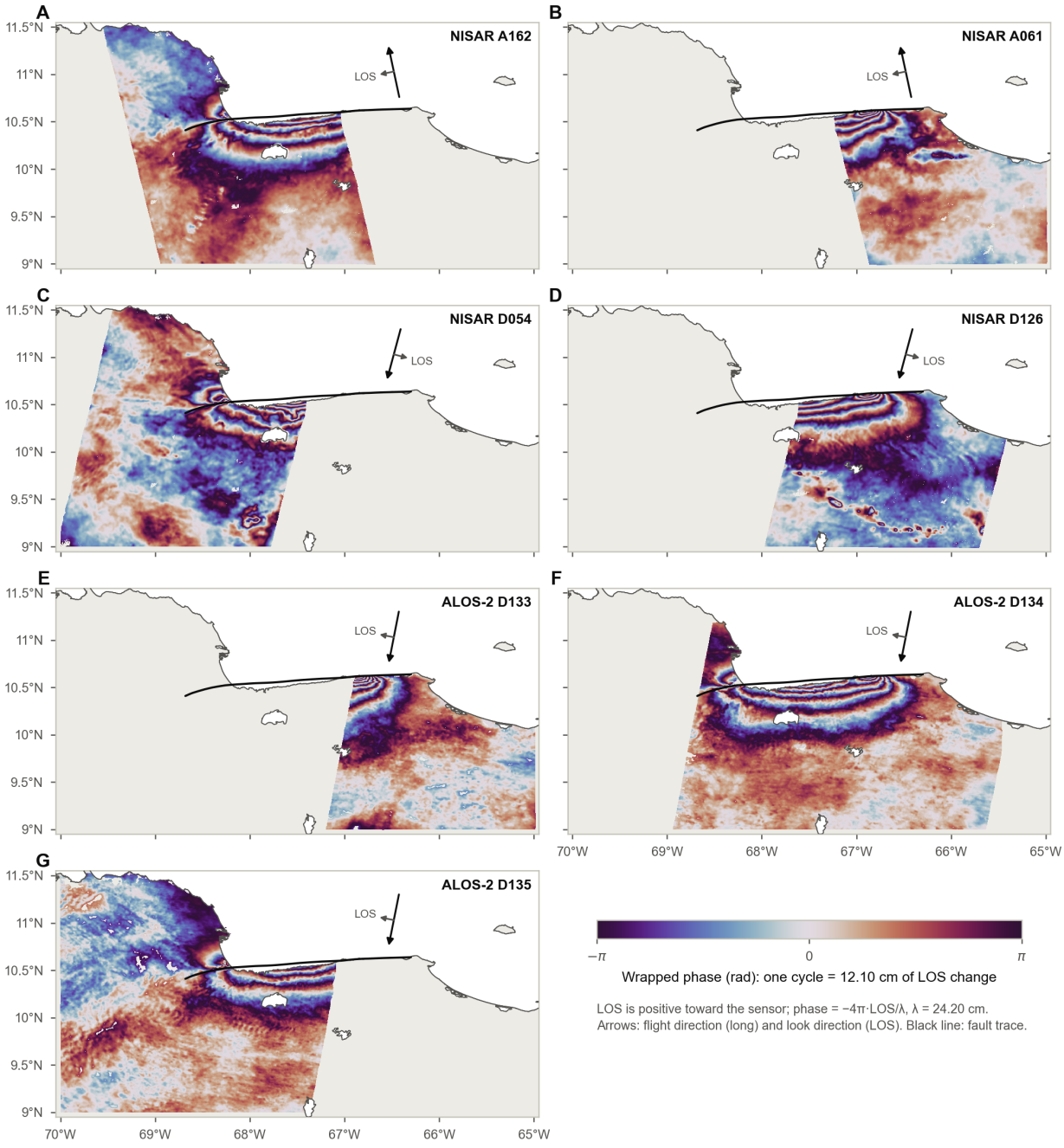


Figure S4: Wrapped NISAR and ALOS-2 interferograms with ionosphere and long-wavelength ramps removed.

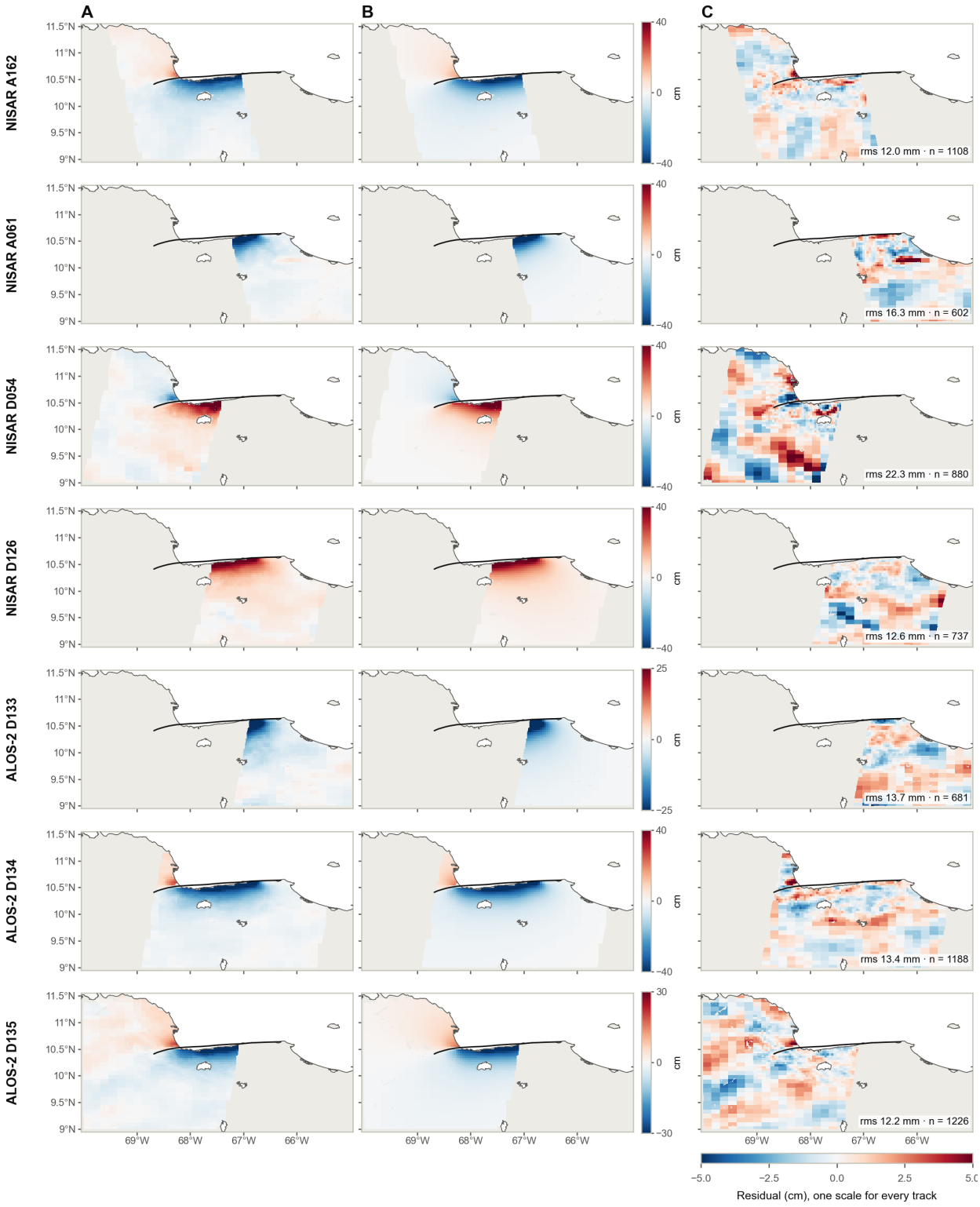


Figure S5: Left column: observed LOS displacements corrected for ionosphere and/or long-wavelength ramps. Middle column: best-fit model predictions. Right column: residuals (data minus model). Black thick line denotes the modeled fault trace.

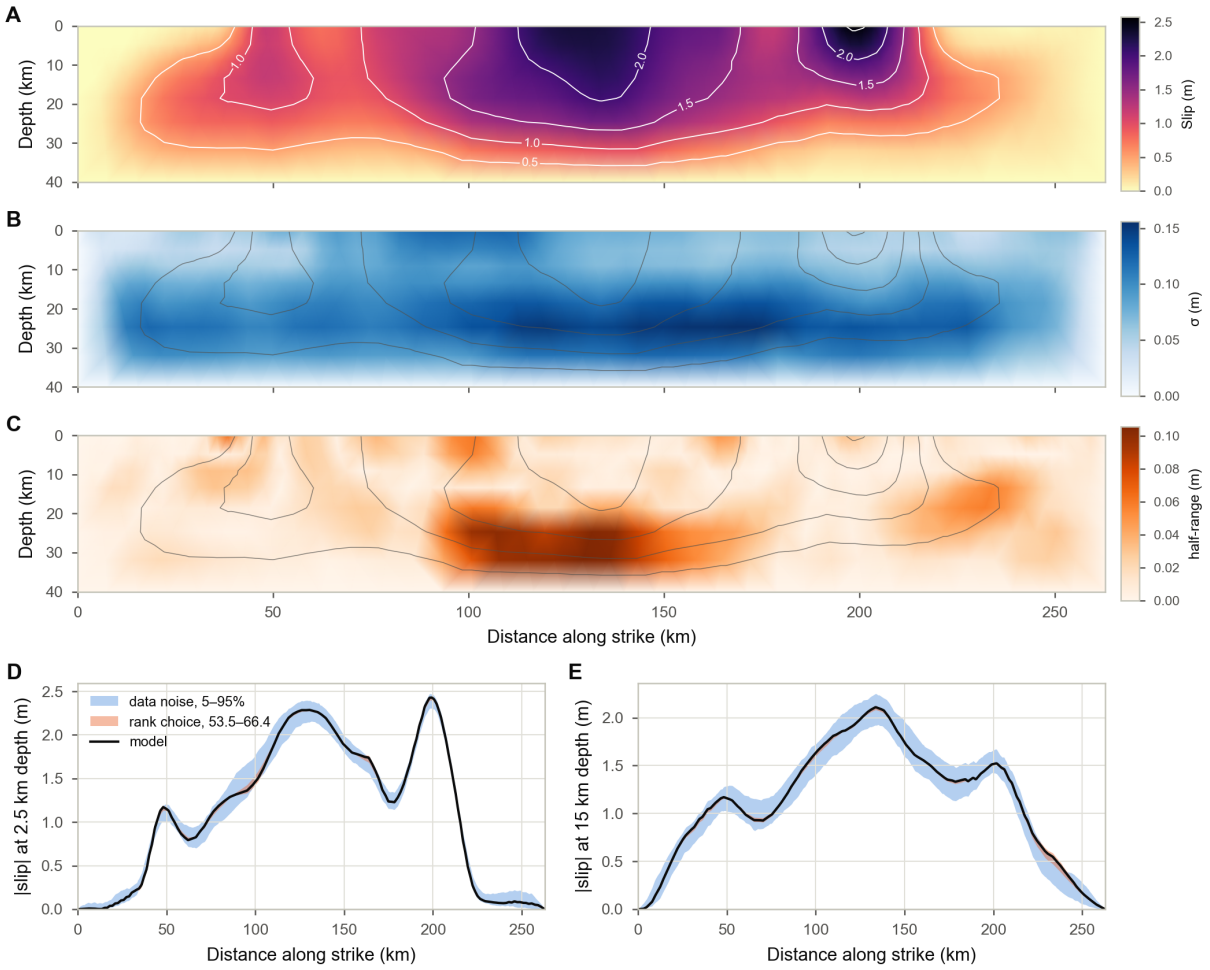


Figure S6: A) Best-fit slip model. Colors and white contours denote the magnitude of coseismic slip, in meters. B) Model uncertainties due to data errors, 1 standard deviation. C) Model uncertainties due to regularization choice, half the distance between the maximum and minimum values. D) Profiles of the two types of uncertainties (B and C) at two depth levels.

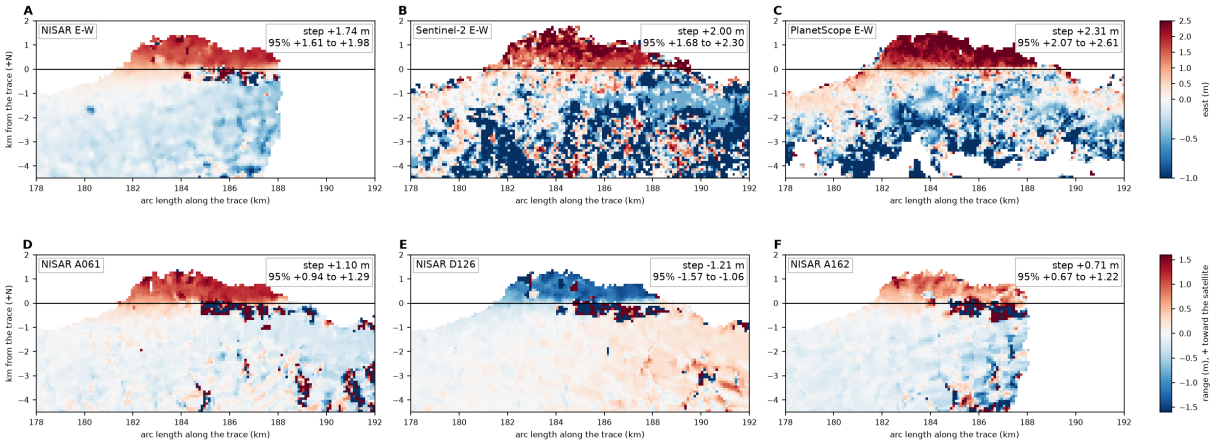


Figure S7: Pixel offsets from NISAR, Sentinel-2, and PlanetScope. a) NISAR east-west offsets obtained from a combination of range offsets from 3 different satellite tracks (shown in panels d-f). b) Sentinel-2 optical east-west offsets. c) PlanetScope optical east-west offsets. d-f) Range offsets from different NISAR tracks.

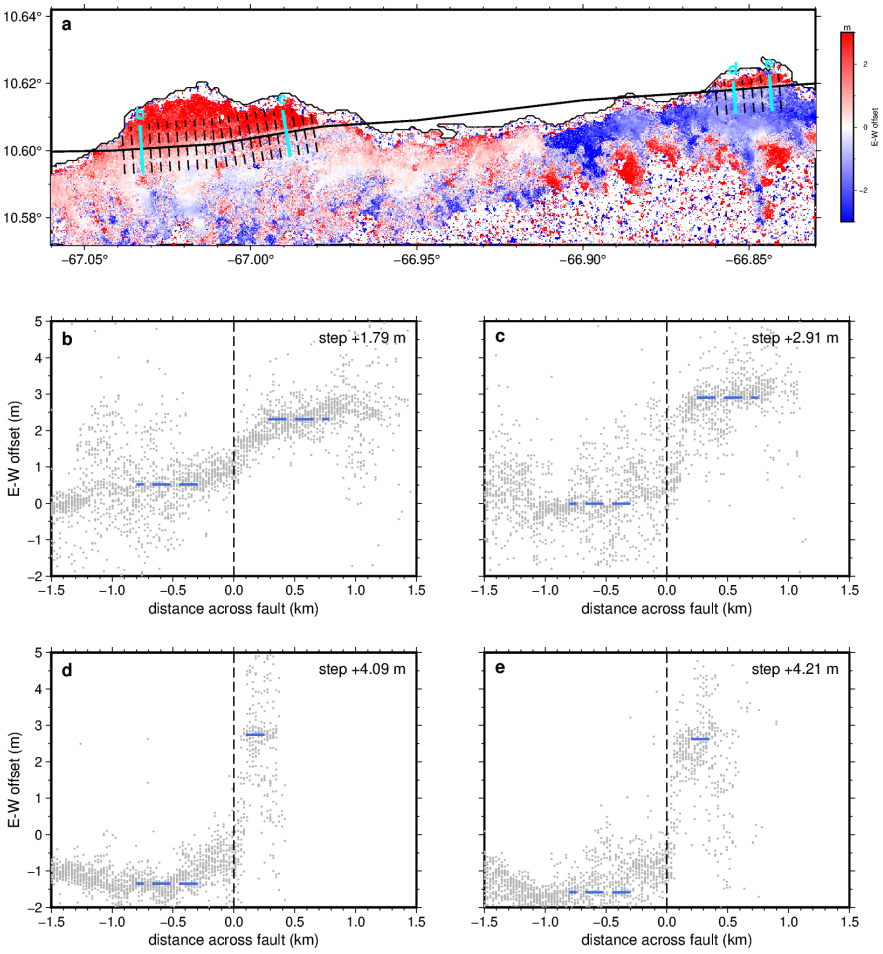


Figure S8: **Near-fault surface displacement from optical image correlation of PlanetScope data.** (a) Map of east–west (E–W) coseismic displacement near Playa Grande and Caraballeda. Black line indicates the mapped fault trace, and the profile locations are shown by black and cyan lines. (b–e) Representative fault-perpendicular displacement profiles extracted from the optical pixel-offset field. Gray dots show displacement measurements, vertical dashed lines mark the fault trace, and horizontal blue dashed lines indicate displacement levels on either side of the fault used to estimate coseismic offsets. The inferred displacement steps are 1.79, 2.91, 4.09, and 4.21 m, respectively.

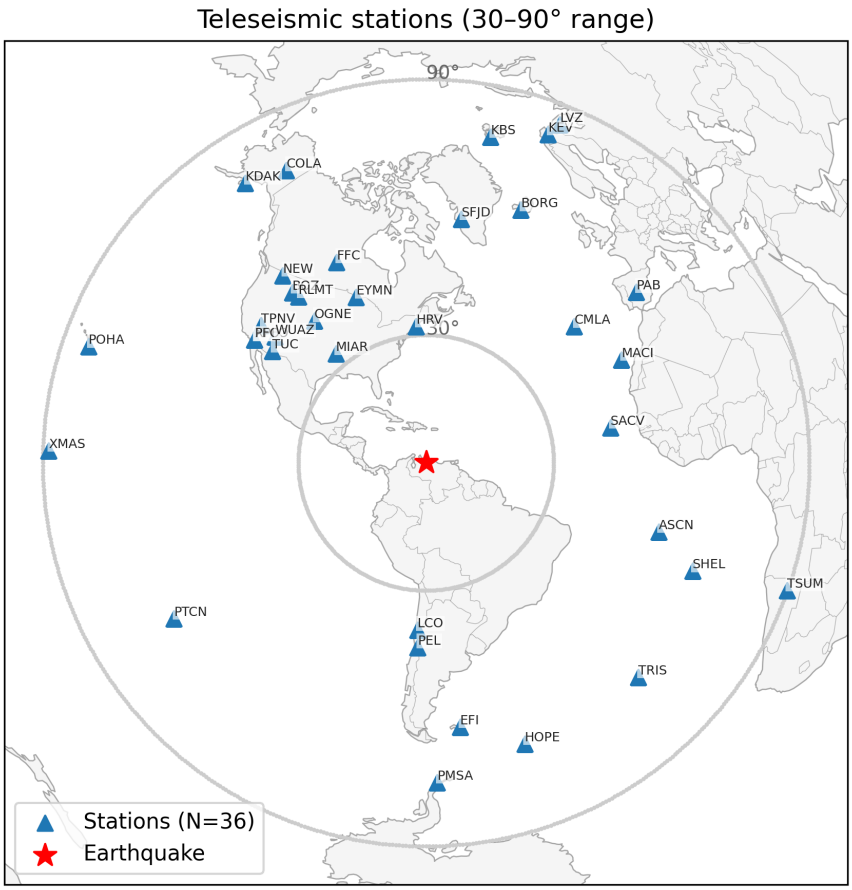


Figure S9: **Teleseismic stations used in the EKI-MultiCMT inversion.** Map view of the 36 stations used for the EKI-MultiCMT inversion.

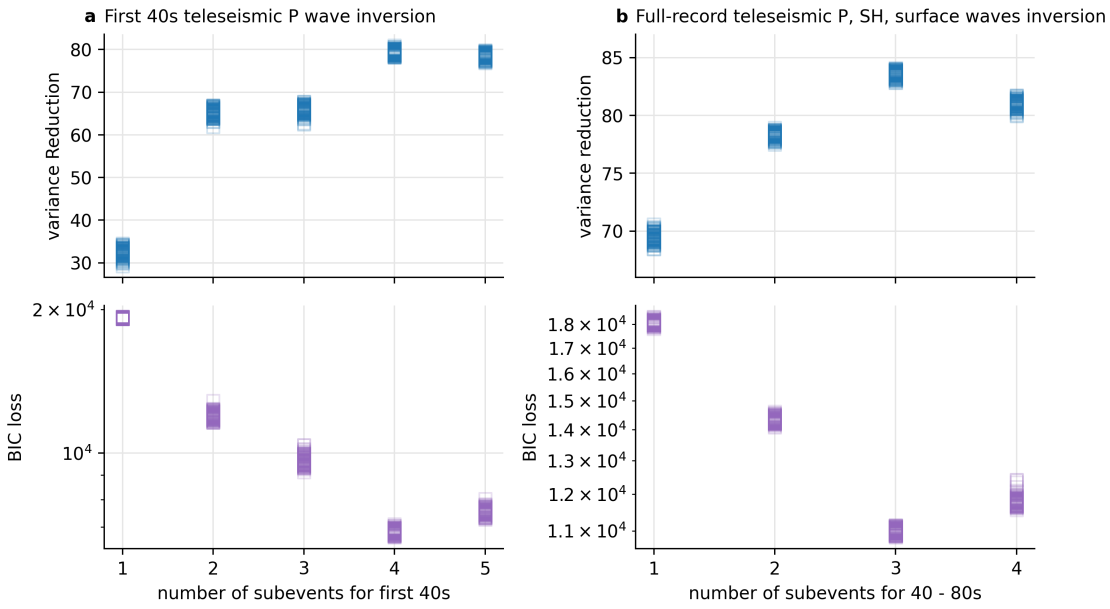


Figure S10: **Comparison of variance reduction and Bayesian Information Criterion (BIC) value with varying number of subevents.** (a) Comparison for the first stage inversion. The four-subevent model achieves the highest variance reduction of 80.0% and the lowest BIC. (b) Comparison for the second-stage inversion. Three additional subevents achieve the highest variance reduction of 83.6% and the lowest BIC.

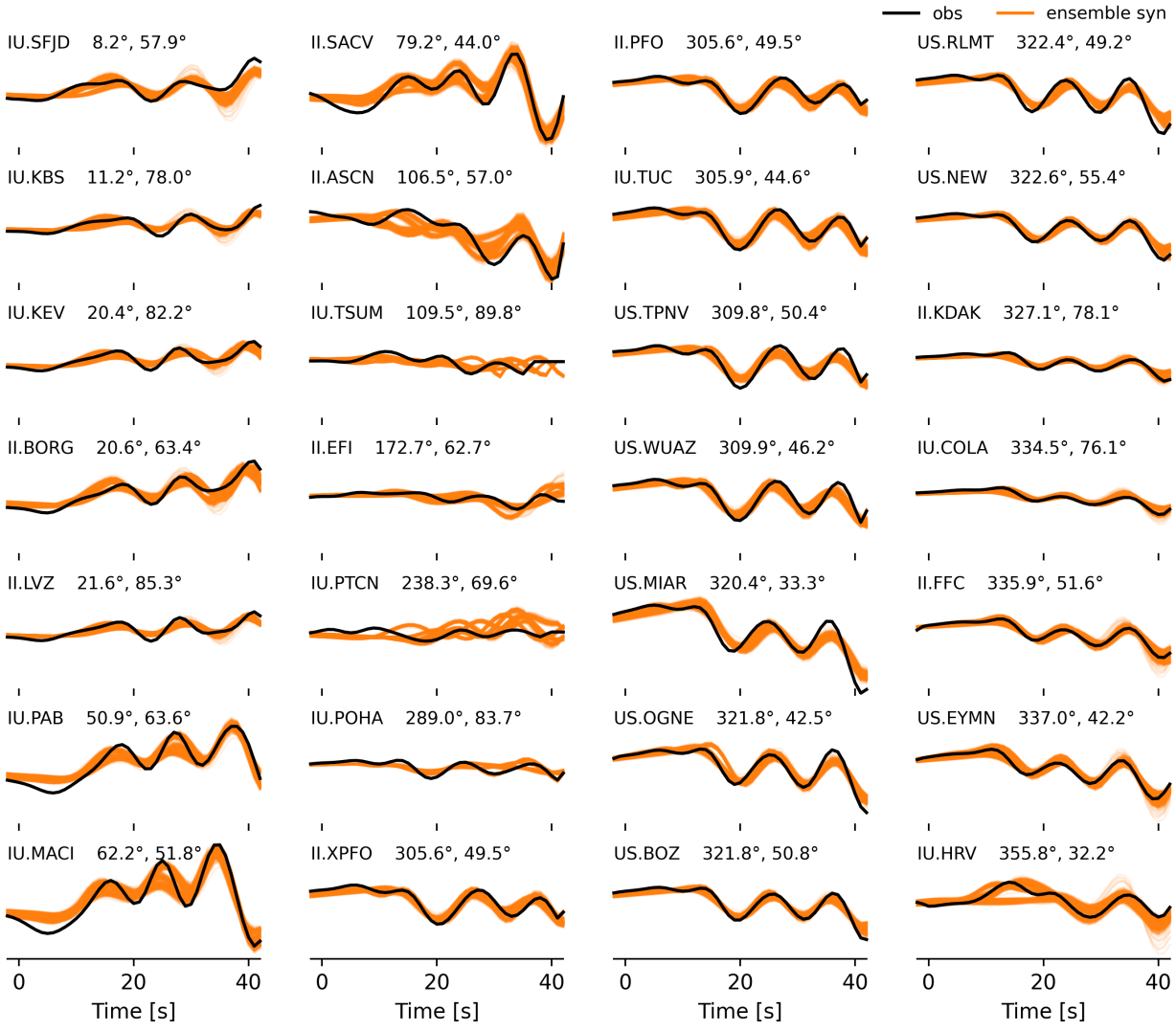


Figure S11: **Comparison of the observed and synthetic teleseismic waveforms of the first inversion.** Black traces show the first 40s of the observed teleseismic P-wave and orange traces show the synthetic waveforms predicted by the EKIMultiCMT ensemble solution. Labels at the top-left corner of each waveform plot show the network, station, azimuth, and station distance in degrees.

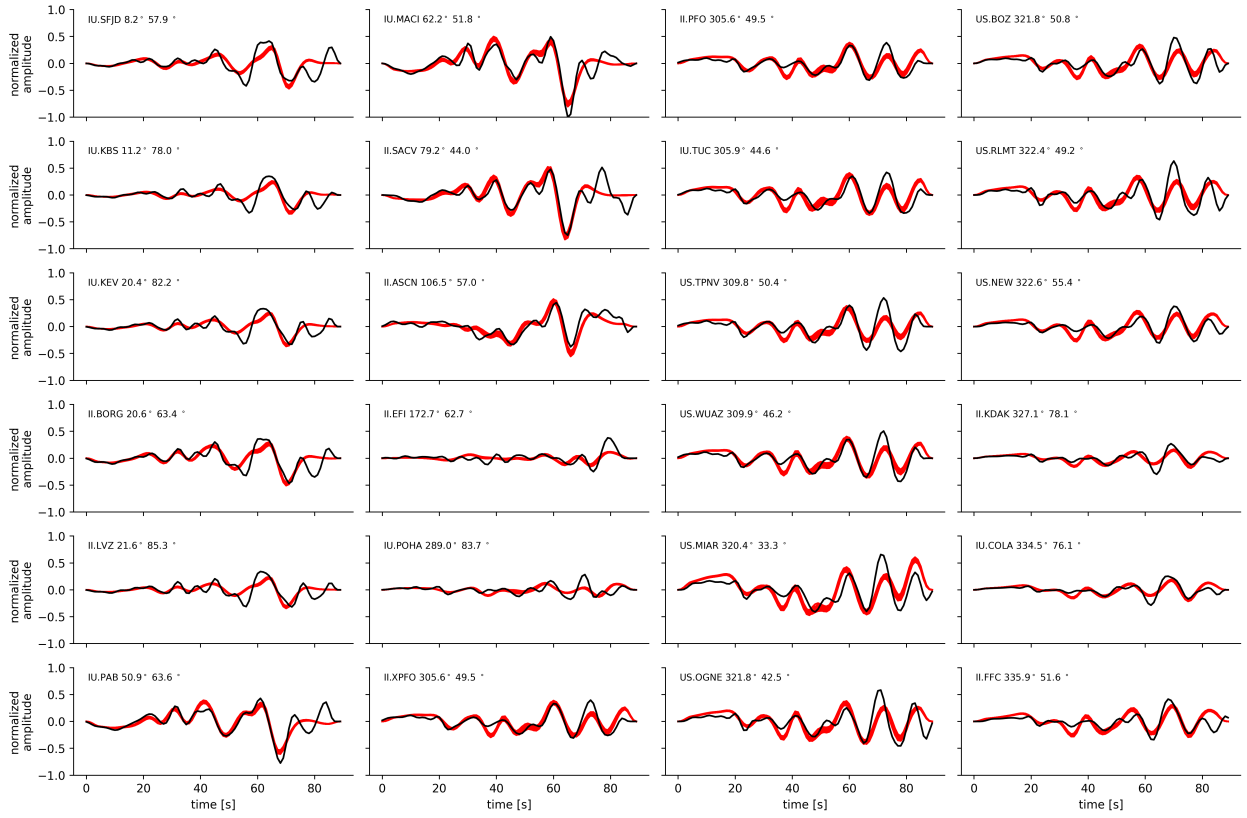


Figure S12: **Comparison of the observed and synthetic teleseismic P waves of the second inversion.** Black traces show the first 80s of the observed teleseismic P-wave and red traces show the synthetic waveforms predicted by the EKIMultiCMT ensemble solution. Labels at the top-left corner of each waveform plot show the network, station, azimuth, and station distance in degrees.

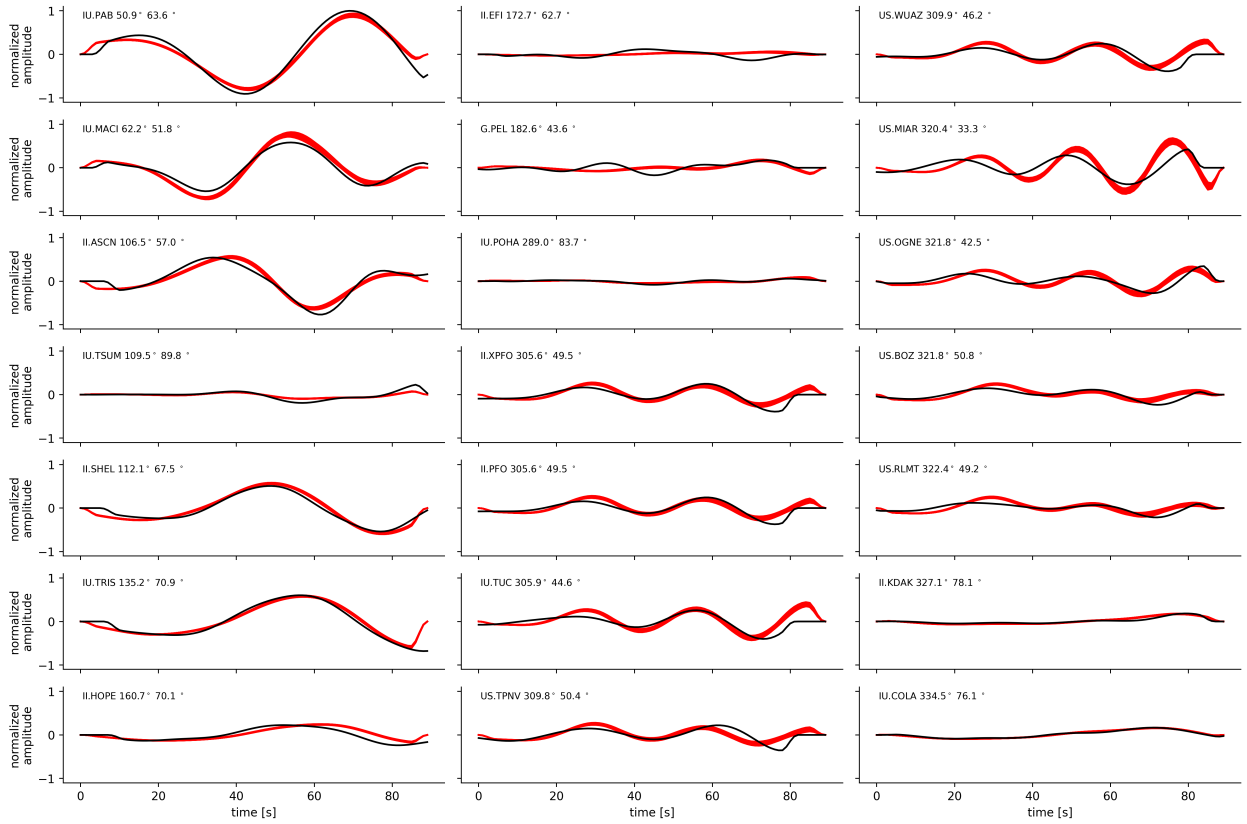


Figure S13: **Comparison of the observed and synthetic teleseismic SH waves of the second inversion.** Black traces show the first 80s of the observed teleseismic SH-wave and red traces show the synthetic waveforms predicted by the EKIMultiCMT ensemble solution. Labels at the top-left corner of each waveform plot show the network, station, azimuth, and station distance in degrees.

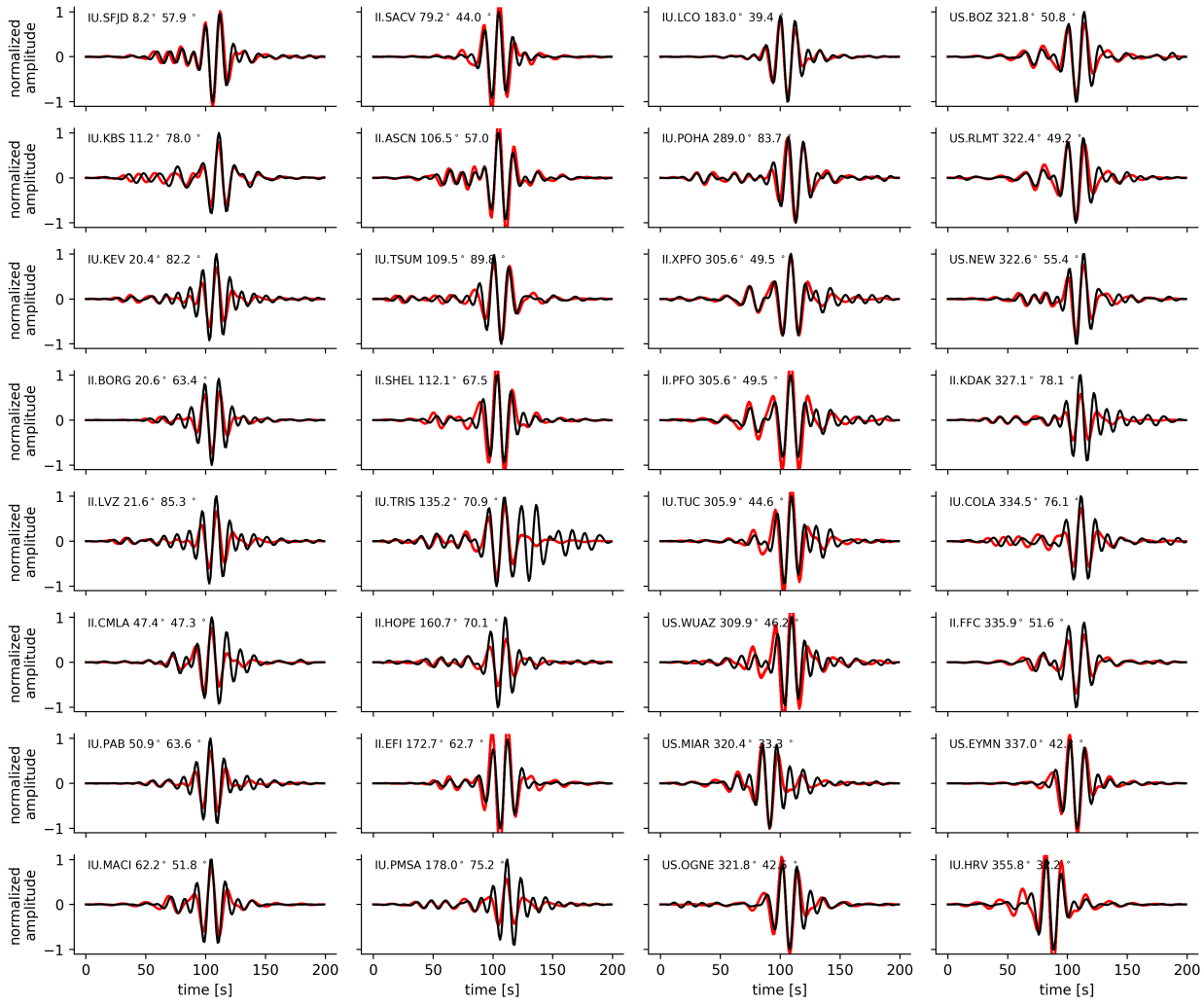


Figure S14: **Comparison of the observed and synthetic teleseismic Love waves of the second inversion.** Black traces show the first 80s of the observed teleseismic Love wave and red traces show the synthetic waveforms predicted by the EKIMultiCMT ensemble solution. Labels at the top-left corner of each waveform plot show the network, station, azimuth, and station distance in degrees.

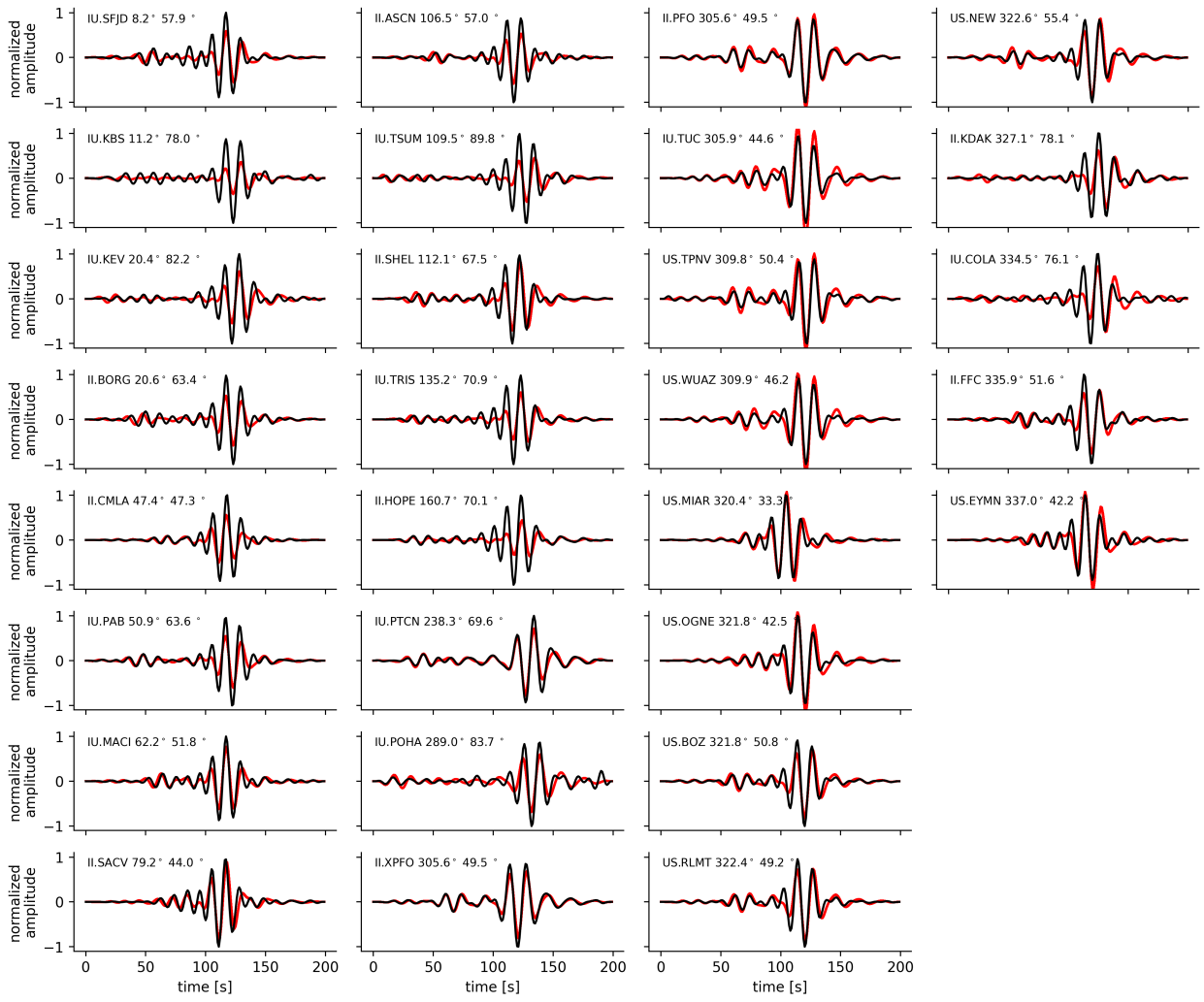


Figure S15: **Comparison of the observed and synthetic teleseismic Rayleigh waves of the second inversion.** Black traces show the first 80s of the observed teleseismic Rayleigh wave and red traces show the synthetic waveforms predicted by the EKIMultiCMT ensemble solution. Labels at the top-left corner of each waveform plot show the network, station, azimuth, and station distance in degrees.

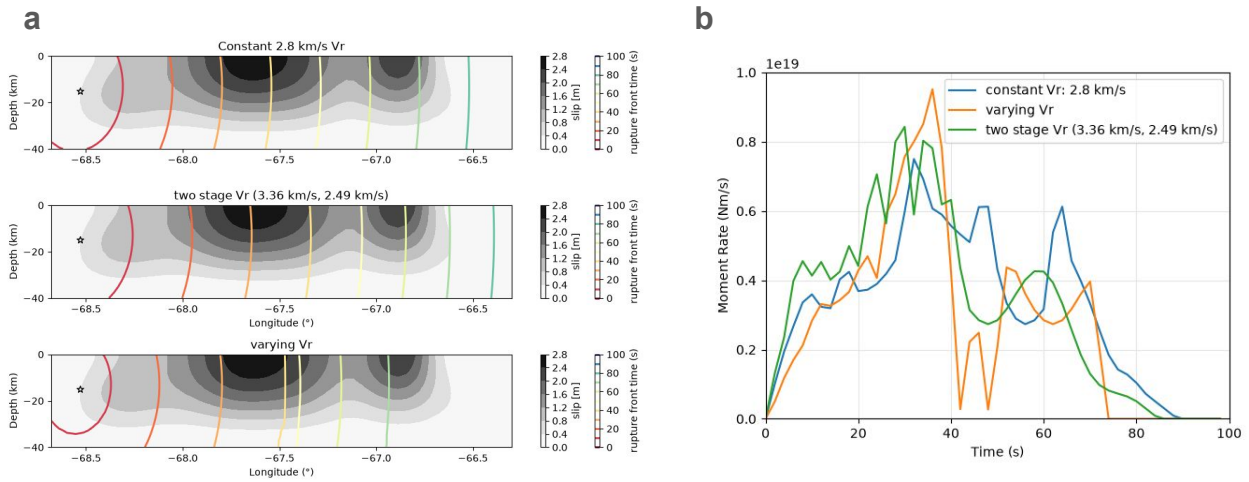


Figure S16: **Comparison of moment-rate function estimates using prescribed rupture speed on a finite-fault slip model.** (a) Comparison of the three assumed rupture propagation patterns with constant 2.8 km/s, 2.49 km/s, and varying rupture speed following the EKI-MultiCMT and backprojection analysis in Fig 3F. (b) Moment-rate function based on the assumed rupture propagation patterns.

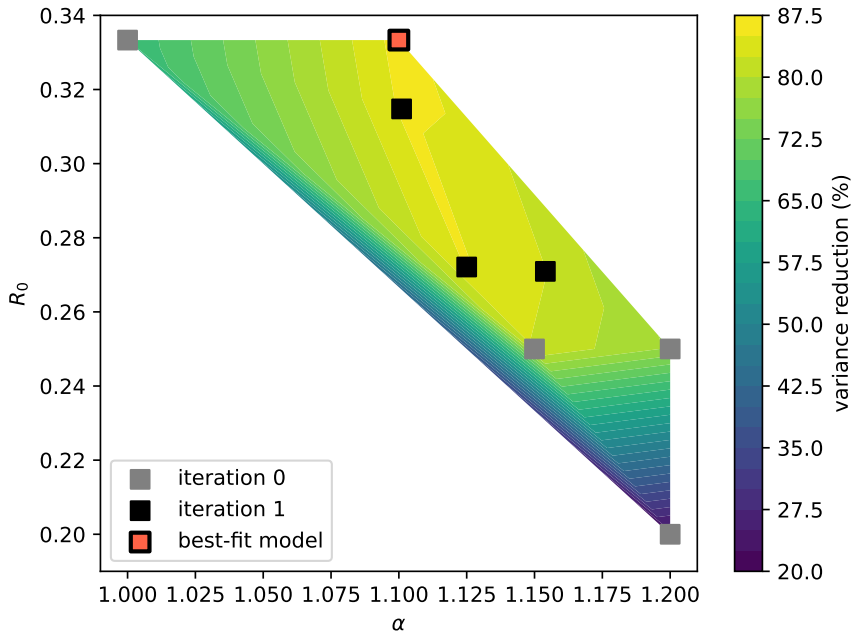


Figure S17: **Ensemble Kalman inversion of the initial stress (α, R_0) parameterization** Geodetic variance reduction as a function of the finite-fault-model stress-scaling factor α and the regional prestress parameter R_0. Colored contours show the interpolated variance reduction across the explored parameter space. Gray squares denote the initial EKI ensemble, black squares denote ensemble members after the first EKI update. The orange outlined square marks the preferred model.

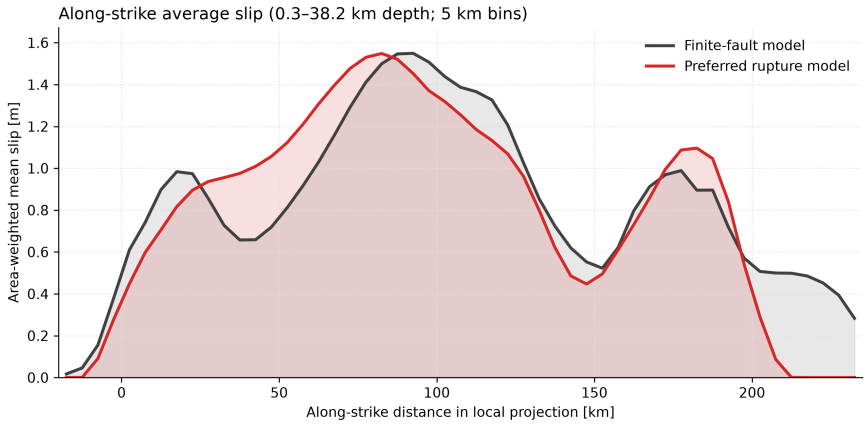


Figure S18: **Along-strike average slip for the finite-fault and preferred dynamic rupture models**. Mean slip is computed in 5-km along-strike bins. Black and red curves show the finite-fault and preferred dynamic rupture models, respectively.

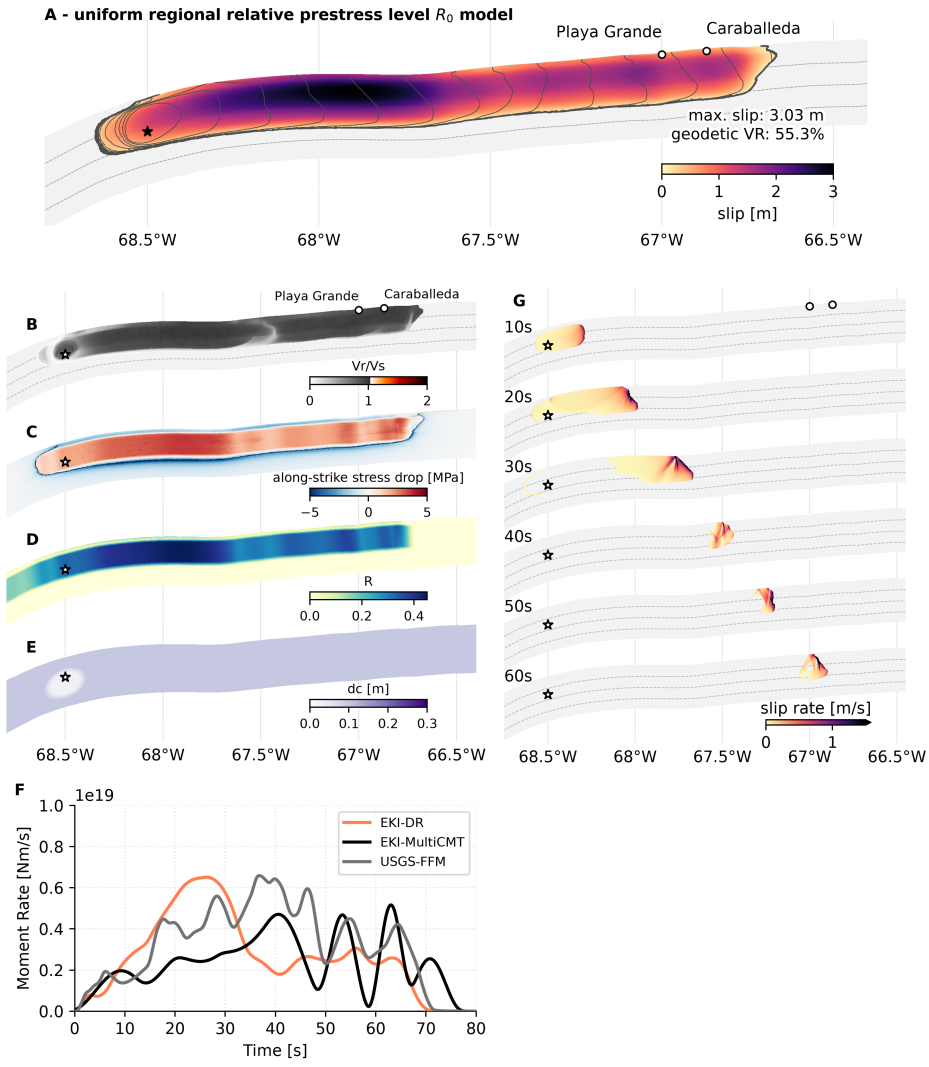


Figure S19: **Dynamic rupture simulation with uniform regional relative prestress level R_0.** Same plotting style as Fig. 4 using the dynamic rupture model with a uniform regional relative prestress level $R_0 = 0.669$.

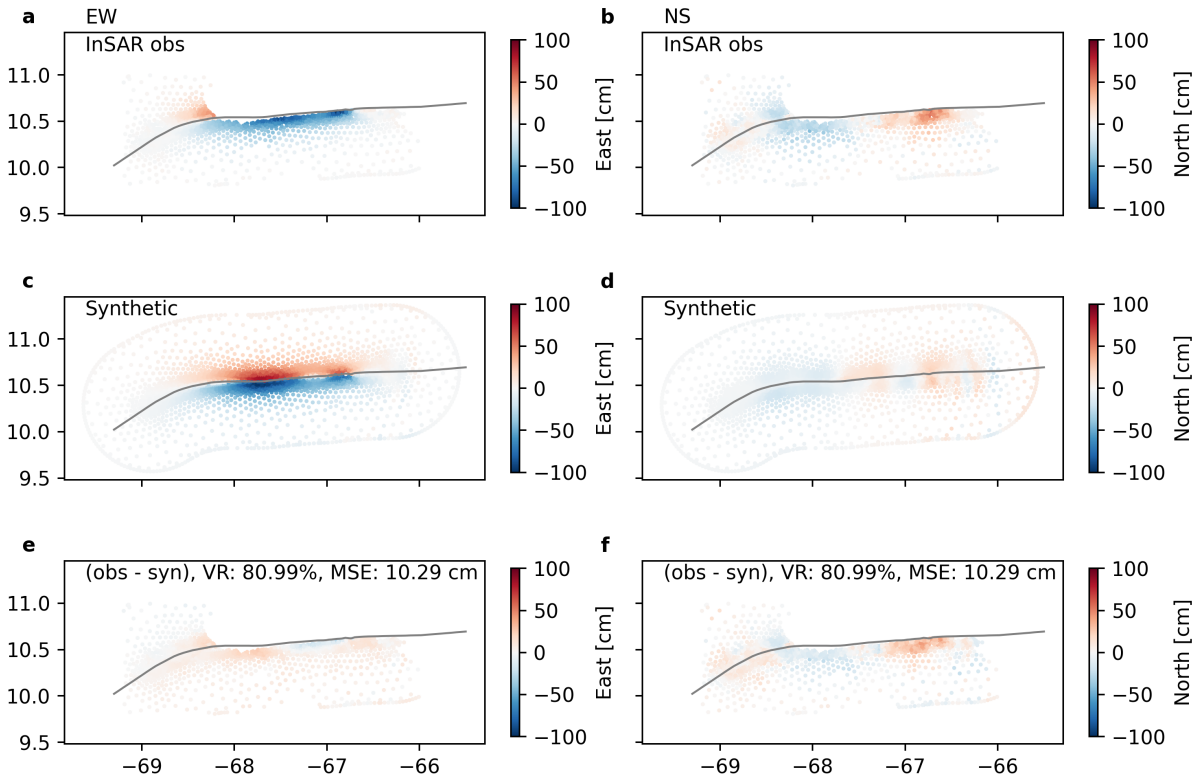


Figure S20: **Geodetic fit of the preferred dynamic rupture model.** (**A,B**) Observed coseismic displacement along the east-west and north-south components, respectively. The data are resampled to dense 1 km spacing near the fault to 10 km spacing 100 km away from the fault trace. (**C,D**) Synthetic east–west surface displacement predicted by the preferred dynamic rupture model. (**E,F**) Residual displacement, calculated as NISAR minus synthetic displacement. The preferred model achieves 81.0% variance reduction and a root-mean-square averaged residual of 10.29 cm. Gray lines indicate the modeled fault trace.

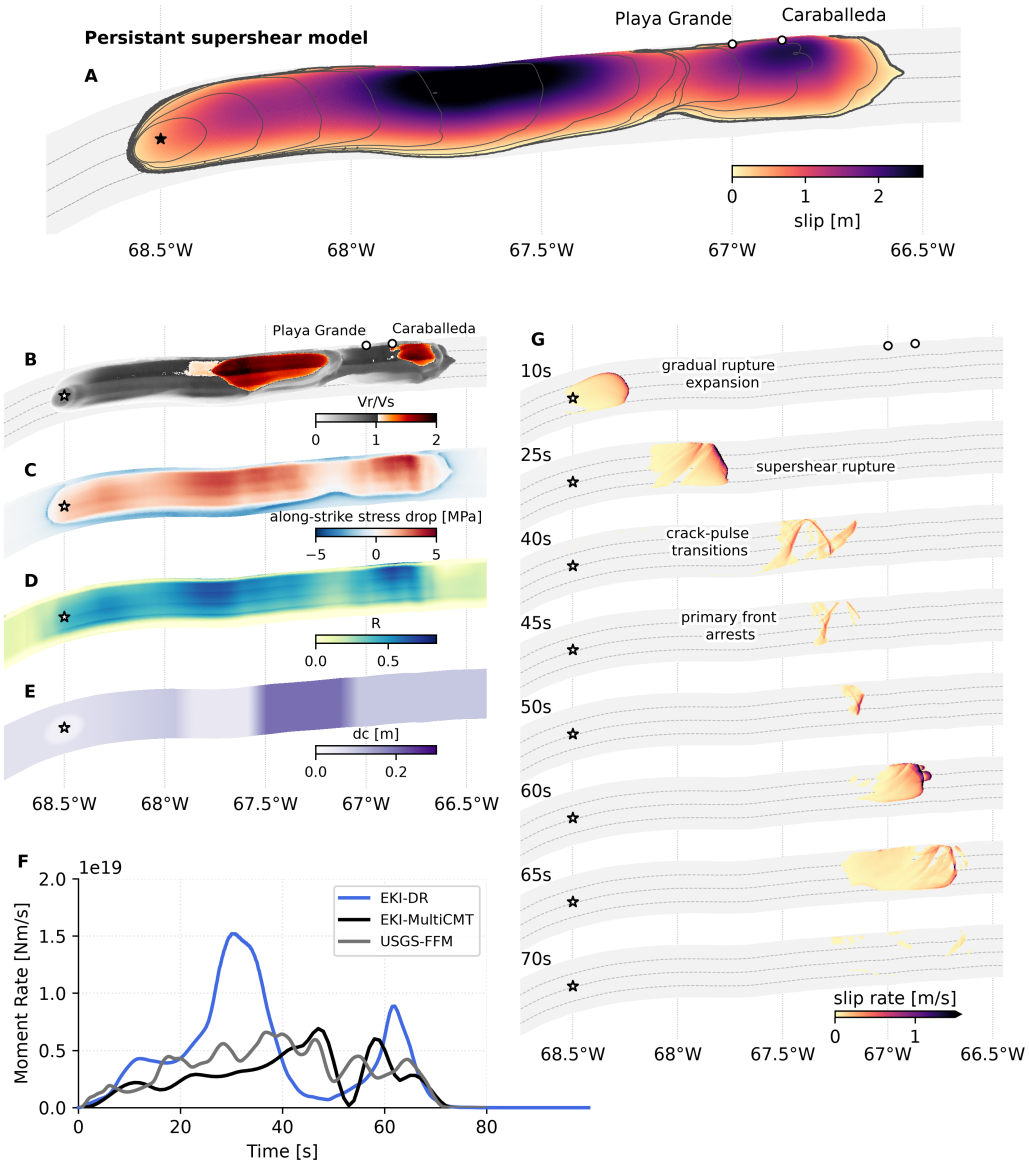


Figure S21: **Alternative dynamic rupture model with persistent supershear rupture. Same plotting style as Fig. 4, for a model with $(R_0, \alpha) = (0.33, 1.2)$ (Table S5). The rupture reaches $V_r/V_s > \sqrt{2}$, and the moment-rate peak exceeds the observed one by more than a factor of two.**

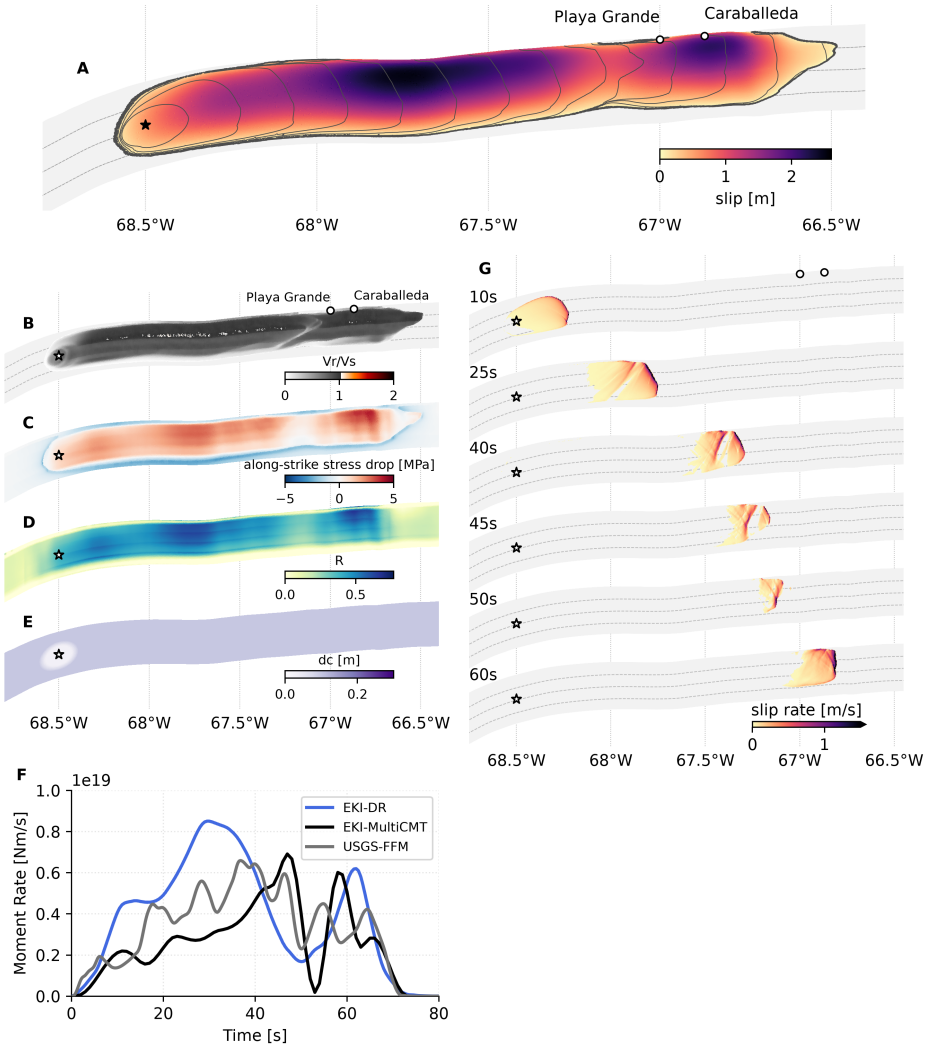


Figure S22: **Dynamic rupture simulation with uniform D_c and heterogeneous prestress with $(R_0, \alpha) = (0.33, 1.1)$.** Same plotting style as Fig. 4 using the dynamic rupture model with a uniform d_c. The entire rupture is subshear.

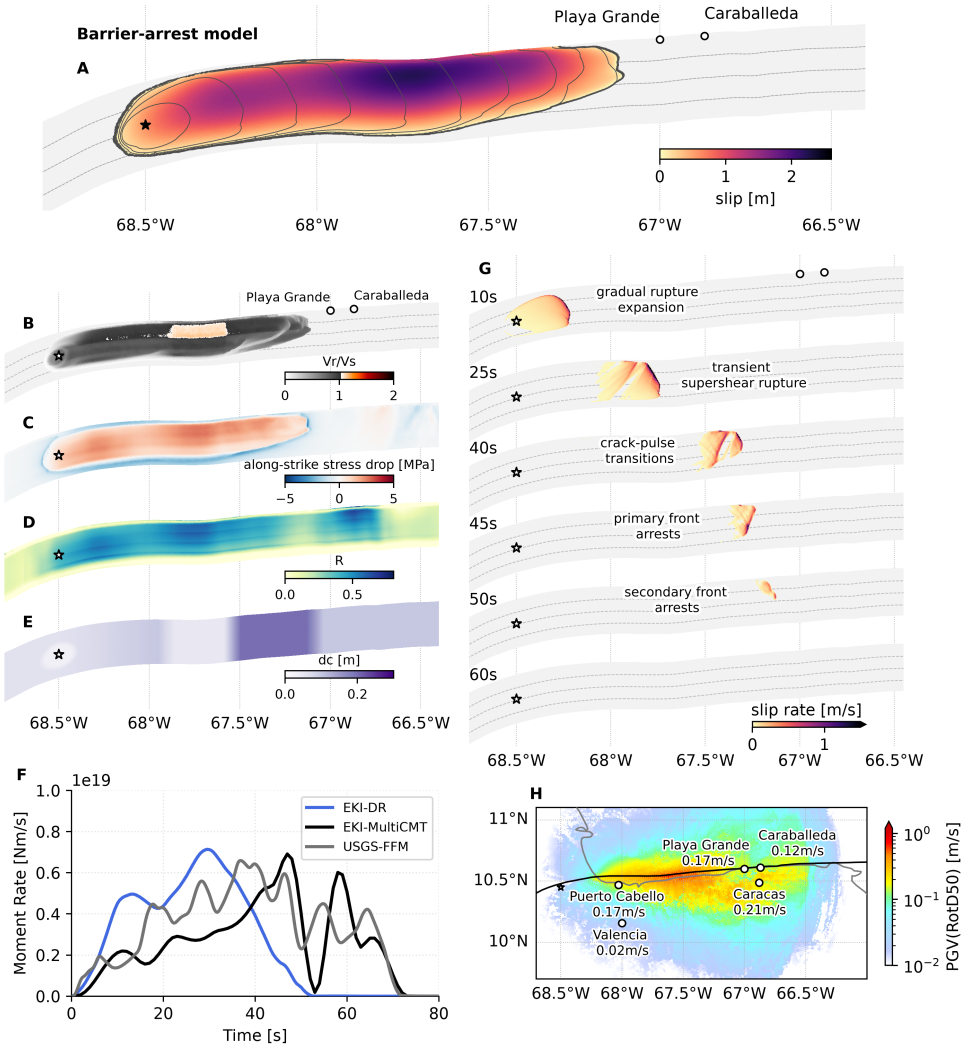


Figure S23: **Dynamic rupture model that arrests at the barrier, with** $(R_0, \alpha) = (0.2, 1.2)$**.** Same plotting style as Fig. 4. Both the primary front and the trailing pulse arrest at the low-stress barrier between the central and eastern asperities, and the earthquake ends as M_w 7.47.

Movie S1. Slip rate evolution of the preferred dynamic rupture model. Fault slip rate of the model in Fig. 4. The color scale gives the slip rate in m/s.

Supplementary References

1. Hayes, G. P. The finite, kinematic rupture properties of great-sized earthquakes since 1990. *Earth and Planetary Science Letters* **468,** 94–100. doi:10.1016/j.epsl.2017.04.003 (2017).

2. *GEOFON Data Centre (GFZ Helmholtz Centere for Geosciences)* 1993. https://doi.org/10.14470/TR560404.

13. Aochi, H. The 1999 Izmit, Turkey, Earthquake: Nonplanar Fault Structure, Dynamic Rupture Process, and Strong Ground Motion. *Bulletin of the Seismological Society of America* **93,** 1249–1266. doi:10.1785/0120020167. (2025) (2003).

17. Ando, R. & Kaneko, Y. Dynamic rupture simulation reproduces spontaneous multifault rupture and arrest during the 2016 Mw 7.9 Kaikoura earthquake. *Geophysical Research Letters* **45,** 12–875 (2018).

18. Ulrich, T., Gabriel, A.-A., Ampuero, J.-P. & Xu, W. Dynamic Viability of the 2016 Mw 7.8 Kaikōura Earthquake Cascade on Weak Crustal Faults. *Nature Communications* **10,** 1213. doi:10.1038/s41467-019-09125-w. (2024) (2019).

21. Jia, Z. *et al.* The Complex Dynamics of the 2023 Kahramanmaraş, Turkey, M_{w} 7.8-7.7 Earthquake Doublet. *Science* **381,** 985–990. doi:10.1126/science.adi0685. (2025) (2023).

27. Fialko, Y., Simons, M. & Agnew, D. The complete (3-D) surface displacement field in the epicentral area of the 1999 M_w7.1 Hector Mine earthquake, southern California, from space geodetic observations. *Geophys. Res. Lett.* **28,** 3063–3066 (2001).

28. Wright, T., Parsons, B. & Lu, Z. Toward mapping surface deformation in three dimensions using InSAR. *Geophys. Res. Lett.* **31,** L01607 (2004).

29. Zou, X. & Fialko, Y. The 2025 Mw 7.1 Tingri (South Tibet) earthquake: Rupture of normal conjugate optimally oriented faults, shallow coseismic slip deficit, and early afterslip. *Seismol. Res. Lett.* **97,** 1667–1680 (2026).

30. Ulrich, T. *et al.* On predictability of slip, rupture geometry, and speed of the 2025 M 7.8 Mandalay, Myanmar, earthquake. *Nature Communications* **17,** 10173 (2026).

31. Wong, J. W. C., Fan, W., Gabriel, A.-A. & Morzfeld, M. *Multi-CMT Inversion of Complex Earthquakes by Ensemble Kalman Optimization* 2026. doi:10.22541/essoar.15007322/v1. (2026).

32. Fan, W. & Shearer, P. M. Detailed rupture imaging of the 25 April 2015 Nepal earthquake using teleseismic P waves. *Geophysical Research Letters* **42,** 5744–5752 (2015).

33. Ishii, M., Shearer, P. M., Houston, H. & Vidale, J. E. Extent, duration and speed of the 2004 Sumatra–Andaman earthquake imaged by the Hi-Net array. *Nature* **435,** 933–936 (2005).

34. Okuwaki, R., Yagi, Y. & Hirano, S. Relationship between high-frequency radiation and asperity ruptures, revealed by hybrid back-projection with a non-planar fault model. *Scientific reports* **4,** 7120 (2014).

35. Andrews, D. Rupture propagation with finite stress in antiplane strain. *Journal of Geophysical Research* **81,** 3575–3582 (1976).

36. Harris, R. A. *et al.* A Suite of Exercises for Verifying Dynamic Earthquake Rupture Codes. *Seismological Research Letters* **89,** 1146–1162. doi:10.1785/0220170222 (2018).

39. Wong, J. W. C., Gabriel, A.-A. & Fan, W. *Evaluating Dynamic Viability of Finite-Fault Slip Models with Ensemble Kalman Inversion* Preprint. 2026. https://eartharxiv.org/repository/view/15466/.

58. Styron, R. & Pagani, M. The GEM global active faults database. *Earthquake Spectra* **36,** 160–180 (2020).

59. SIGGMA. *Preliminary GNSS evidence of coseismic deformation in Caracas associated with the 24 June 2026 earthquake* Last accessed: 2026-07-27. 2026. https://siggma.xyz/preliminary-gnss-evidence-earthquake-caracas/.

60. Boore, D. M. Orientation-independent, nongeometric-mean measures of seismic intensity from two horizontal components of motion. *Bulletin of the Seismological Society of America* **100,** 1830–1835 (2010).

65. Sandwell, D., Mellors, R., Tong, X., Wei, M. & Wessel, P. Open radar interferometry software for mapping surface deformation. *Eos, Trans. AGU* **92,** 234–234 (2011).

66. Farr, T. & Kobrick, M. Shuttle Radar Topography Mission produces a wealth of data. *AGU Eos* **81,** 583–585 (2000).

67. Goldstein, R. M., Zebker, H. A. & Werner, C. L. Satellite radar interferometry: Two-dimensional phase unwrapping. *Radio science* **23,** 713–720 (1988).

68. Chen, C. & Zebker, H. A. Two-dimensional phase unwrapping with use of statistical models for cost functions in nonlinear optimization. *Journal of the Optical Society of America. A, Optics, image science, and vision* **18,** 338–51. doi:10.1364/JOSAA.18.000338 (2001).

69. Fialko, Y. & Jin, Z. Simple shear origin of the cross-faults ruptured in the 2019 Ridgecrest earthquake sequence. *Nature Geoscience* **14,** 513–518 (2021).

70. Fialko, Y., Sandwell, D., Simons, M. & Rosen, P. Three-dimensional deformation caused by the Bam, Iran, earthquake and the origin of shallow slip deficit. *Nature* **435,** 295–299 (2005).

71. Leprince, S., Barbot, S., Ayoub, F. & Avouac, J.-P. Automatic and precise orthorectification, coregistration, and subpixel correlation of satellite images, application to ground deformation measurements. *IEEE Transactions on Geoscience and Remote Sensing* **45,** 1529–1558 (2007).

72. Aati, S., Milliner, C. & Avouac, J.-P. A new approach for 2-D and 3-D precise measurements of ground deformation from optimized registration and correlation of optical images and ICA-based filtering of image geometry artifacts. *Remote Sensing of Environment* **277,** 113038 (2022).

73. Buades, A., Coll, B. & Morel, J.-M. Nonlocal Image and Movie Denoising. *International journal of computer vision* **76,** 123–139. doi:10.1007/s11263-007-0052-1 (2008).

74. Ayoub, F., Leprince, L. & Avouac, J. *User's guide to COSI-CORR: Co-registration of optically sensed images and correlation, California Institute of Technology* 2015.

75. Milliner, C., Avouac, J., Dolan, J. & Hollingsworth, J. Localization of inelastic strain with fault maturity and effects on earthquake characteristics. *Nature Geoscience* **18,** 793–800 (2025).

76. Fialko, Y. Probing the mechanical properties of seismically active crust with space geodesy: Study of the co-seismic deformation due to the 1992 M_w7.3 Landers (southern California) earthquake. *J. Geophys. Res.* **109,** B03307 (2004).

77. Barnhart, W. D. & Lohman, R. B. Automated fault model discretization for inversions for coseismic slip distributions. *Journal of Geophysical Research: Solid Earth* **115.** doi:https://doi.org/10.1029/2010JB007545 (2010).

78. Zienkiewicz, O. *The Finite Element Method* 3rd ed. (McGraw-Hill Book Company, London, 1977).

79. Golub, G. H., Hansen, P. C. & O'Leary, D. P. Tikhonov regularization and total least squares. *SIAM journal on matrix analysis and applications* **21,** 185–194 (1999).

80. Meyer, M., Desbrun, M., Schröder, P. & Barr, A. H. in *Visualization and mathematics III* 35–57 (Springer, 2003).

81. Feng, G. & Jónsson, S. Shortcomings of InSAR for studying megathrust earthquakes: The case of the Mw9.0 Tohoku-Oki earthquake. *Geophysical Research Letters* **39,** L10305. doi:10.1029/2012GL051628 (2012).

82. Jin, Z. & Fialko, Y. Finite slip models of the 2019 Ridgecrest earthquake sequence constrained by space geodetic data and aftershock locations. *Bull. Seism. Soc. Am.* **110,** 1660–1679 (2020).

83. Matthews, M. V. & Segall, P. Estimation of depth-dependent fault slip from measured surface deformation with application to the 1906 San Francisco earthquake. *Journal of Geophysical Research* **98,** 12153–12163. doi:10.1029/93JB00440 (1993).

84. Kennett, B. & Engdahl, E. Traveltimes for global earthquake location and phase identification. *Geophysical Journal International* **105,** 429–465 (1991).

85. Rost, S. & Thomas, C. Array seismology: Methods and applications. *Reviews of Geophysics* **40,** 1008. doi:10.1029/2000RG000100 (2002).

86. Xu, Y., Koper, K. D., Sufri, O., Zhu, L. & Hutko, A. R. Rupture imaging of the Mw 7.9 12 May 2008 Wenchuan earthquake from back projection of teleseismic P waves. *Geochemistry, Geophysics, Geosystems* **10,** Q04006. doi:10.1029/2008GC002335 (2009).

87. Tsai, V. C., Nettles, M., Ekström, G. & Dziewonski, A. M. Multiple CMT source analysis of the 2004 Sumatra earthquake. *Geophysical Research Letters* **32** (2005).

88. Iglesias, M. A., Law, K. J. H. & Stuart, A. M. Ensemble Kalman Methods for Inverse Problems. *Inverse Problems* **29,** 045001. doi:10.1088/0266-5611/29/4/045001. (2025) (2013).

89. Van Driel, M., Krischer, L., Stähler, S. C., Hosseini, K. & Nissen-Meyer, T. Instaseis: instant global seismograms based on a broadband waveform database. *Solid Earth* **6,** 701–717 (2015).

90. Krischer, L. *et al.* On-demand custom broadband synthetic seismograms. *Seismological Research Letters* **88,** 1127–1140 (2017).

91. Premus, J. & Ampuero, J. P. Dynamic earthquake source inversion with Generative Adversarial Network priors. *Journal of Geophysical Research: Solid Earth* **131,** e2025JB033232 (2026).

92. Chada, N. K., Stuart, A. M. & Tong, X. T. Tikhonov regularization within ensemble Kalman inversion. *SIAM Journal on Numerical Analysis* **58,** 1263–1294 (2020).

93. Kitanidis, P. K. Quasi-linear geostatistical theory for inversing. *Water Resources Research* **31,** 2411–2419. doi:10.1029/95WR01945 (1995).

94. Oliver, D. S., He, N. & Reynolds, A. C. *Conditioning Permeability Fields to Pressure Data* in *5th European Conference on the Mathematics of Oil Recovery (ECMOR V)* (European Association of Geoscientists & Engineers, 1996). doi:10.3997/2214-4609.201406884.

95. Blatter, D., Morzfeld, M., Key, K. & Constable, S. Uncertainty quantification for regularized inversion of electromagnetic geophysical data—Part I: motivation and theory. *Geophysical Journal International* **231,** 1057–1074 (2022).

96. Andrews, D. J. Rupture Dynamics with Energy Loss Outside the Slip Zone. *Journal of Geophysical Research: Solid Earth* **110.** doi:10.1029/2004JB003191 (2005).

97. Ramos, M. D., Thakur, P., Huang, Y., Harris, R. A. & Ryan, K. J. Working with dynamic earthquake rupture models: A practical guide. *Seismological Society of America* **93,** 2096–2110 (2022).

98. Gabriel, A.-A. *et al. SeisSol* Zenodo. 2025. doi:10.5281/zenodo.15685917.

99. Dumbser, M. & Käser, M. An Arbitrary High-Order Discontinuous Galerkin Method for Elastic Waves on Unstructured Meshes — II. The Three-Dimensional Isotropic Case. *Geophysical Journal International* **167,** 319–336. doi:10.1111/j.1365-246X.2006.03120.x. (2024) (2006).

100. Pelties, C., Gabriel, A.-A. & Ampuero, J.-P. Verification of an ADER-DG Method for Complex Dynamic Rupture Problems. *Geoscientific Model Development* **7,** 847–866. doi:10.5194/gmd-7-847-2014. (2024) (2014).

101. Bassin, C. The current limits of resolution for surface wave tomography in North America. *Eos Trans. AGU* **81,** F897 (2000).

102. GEBCO Bathymetric Compilation Group 2026. *The GEBCO_2026 Grid – A Continuous Terrain Model for Oceans and Land at 15 Arc-Second Intervals* 2026. doi:10.5285/4f68d5c7-45eb-f999-e063-7086abc036fa.

103. Wollherr, S., Gabriel, A.-A. & Uphoff, C. Off-fault plasticity in three-dimensional dynamic rupture simulations using a modal Discontinuous Galerkin method on unstructured meshes: implementation, verification and application. *Geophysical Journal International* **214,** 1556–1584 (2018).

104. Stanzione, D. *et al.* in *Practice and experience in advanced research computing 2020: Catch the wave* 106–111 (2020).

105. Ida, Y. Cohesive force across the tip of a longitudinal-shear crack and Griffith's specific surface energy. *Journal of Geophysical Research* **77,** 3796–3805 (1972).

106. Peyrat, S., Olsen, K. & Madariaga, R. Dynamic modeling of the 1992 Landers earthquake. *Journal of Geophysical Research: Solid Earth* **106,** 26467–26482 (2001).

107. Premus, J., Gallovič, F. & Ampuero, J.-P. Bridging time scales of faulting: From coseismic to postseismic slip of the M w 6.0 2014 South Napa, California earthquake. *Science advances* **8,** eabq2536 (2022).

108. Li, B. *et al.* Seismic gap breached by the 2025 M w 7.7 Mandalay (Myanmar) earthquake. *Nature Geoscience* **18,** 1287–1295 (2025).

109. Yin, H., Marchandon, M., Haase, J., Gabriel, A.-A. & Douilly, R. *3D Dynamic Rupture Modeling of the 2021 Haiti Earthquake Used to Constrain Stress Conditions and Fault System Complexity* 2025. doi:10.31223/X5NM75. (2026).

110. Rice, J. R. in *Fault Mechanics and Transport Properties of Rocks* (eds Evans, B. & Wong, T.-f.) 475–503 (Academic Press, 1992). doi:https://doi.org/10.1016/S0074-6142(08)62835-1.

111. Drucker, D. C. & Prager, W. Soil mechanics and plastic analysis or limit design. *Quarterly of applied mathematics* **10,** 157–165 (1952).

112. Templeton, E. L. & Rice, J. R. Off-Fault Plasticity and Earthquake Rupture Dynamics: 1. Dry Materials or Neglect of Fluid Pressure Changes. *Journal of Geophysical Research: Solid Earth* **113.** doi:10.1029/2007JB005529 (2008).

113. Wollherr, S., Gabriel, A.-A. & Uphoff, C. Off-Fault Plasticity in Three-Dimensional Dynamic Rupture Simulations Using a Modal Discontinuous Galerkin Method on Unstructured Meshes: Implementation, Verification and Application. *Geophysical Journal International* **214,** 1556–1584. doi:10.1093/gji/ggy213 (2018).

114. Shi, Z. & Day, S. M. Rupture dynamics and ground motion from 3-D rough-fault simulations. *Journal of Geophysical Research: Solid Earth* **118,** 1122–1141 (2013).

115. Roten, D., Olsen, K. B., Day, S. M., Cui, Y. & Fäh, D. Expected seismic shaking in Los Angeles reduced by San Andreas fault zone plasticity. *Geophysical Research Letters* **41,** 2769–2777 (2014).

116. Anderson, E. M. *The Dynamics of Faulting and Dyke Formation with Applications to Britain* 2nd ed. (Oliver and Boyd, Edinburgh, 1951).

117. Heidbach, O. *et al.* The World Stress Map database release 2016: Crustal stress pattern across scales. *Tectonophysics* **744,** 484–498 (2018).

118. Audemard M, F., Singer P, A. & Soulas, J.-P. Quaternary faults and stress regime of Venezuela. *Revista de la Asociación Geológica Argentina* **61,** 480–491 (2006).